AGU PUBLICATIONS

JGR

Journal of Geophysical Research: Earth Surface

RESEARCH ARTICLE
10.1002/2015JF003662

Key Points:
- Rock damage associated with shear abrasion locally enhances erodibility and transport of substrate
- Rapid erosion of weak zones causes accumulation of coarse sediments from adjacent sources
- Sediment residence time scales with erodibility of weak zone

Supporting Information:
- Supporting Information S1

Correspondence to:
S. G. Roy,
Samuel.g.roy@maine.edu

Citation:
Roy, S. G., G. E. Tucker, P. O. Koons, S. M. Smith, and P. Upton (2016), A fault runs through it: Modeling the influence of rock strength and grain-size distribution in a fault-damaged landscape, *J. Geophys. Res. Earth Surf.*, *121*, 1911–1930, doi:10.1002/2015JF003662.

Received 2 JUL 2015
Accepted 6 OCT 2016
Accepted article online 13 OCT 2016
Published online 22 OCT 2016

A fault runs through it: Modeling the influence of rock strength and grain-size distribution in a fault-damaged landscape

S. G. Roy[1,3], G. E. Tucker[2], P. O. Koons[3], S. M. Smith[1,3], and P. Upton[3,4]

[1]George J. Mitchell Center for Sustainability Solutions, University of Maine, Orono, Maine, USA, [2]Cooperative Institute for Research in Environmental Sciences and Department of Geological Sciences, University of Colorado Boulder, Boulder, Colorado, USA, [3]School of Earth and Climate Sciences, University of Maine, Orono, Maine, USA, [4]GNS Science, Lower Hutt, New Zealand

Abstract We explore two ways in which the mechanical properties of rock potentially influence fluvial incision and sediment transport within a watershed: rock erodibility is inversely proportional to rock cohesion, and fracture spacing influences the initial grain sizes produced upon erosion. Fault-weakened zones show these effects well because of the sharp strength gradients associated with localized shear abrasion. A natural example of fault erosion is used to motivate our calibration of a generalized landscape evolution model. Numerical experiments are used to study the sensitivity of river erosion and transport processes to variable degrees of rock weakening. In the experiments, rapid erosion and transport of fault gouge steers surface runoff, causing high-order channels to become confined within the structure of weak zones when the relative degree of rock weakening exceeds 1 order of magnitude. Erosion of adjacent, intact bedrock produces relatively coarser grained gravels that accumulate in the low relief of the eroded weak zone. The thickness and residence time of sediments stored there depends on the relief of the valley, which in these models depends on the degree of rock weakening. The frequency with which the weak zone is armored by bed load increases with greater weakening, causing the bed load to control local channel slope. Conversely, small tributaries feeding into the weak zone are predominantly detachment limited. Our results indicate that mechanical heterogeneity can exert strong controls on rates and patterns of erosion and should be considered in future landscape evolution studies to better understand the role of heterogeneity in structuring landscapes.

1. Introduction

Mechanical defects such as faults, joints, and fractures are commonplace in the brittle crust, and there is clear evidence that their existence and distribution influence rates and patterns of erosion. Some have argued that brittle failure is the first step in erosion and is therefore fundamental to all landscape evolution processes [e.g., *Gilbert*, 1877; *Davis*, 1899; *Scheidegger*, 1979, 2001, 2004; *Molnar et al.*, 2007; *Koons et al.*, 2012; *Sklar et al.*, 2016]. Mechanical defects influence surface processes in at least two ways. First, the presence of defects such as fractures and joints facilitates rock disaggregation and particle removal; greater defect frequency leads to smaller blocks that are more easily dislodged by various geomorphological processes [e.g., *Molnar et al.*, 2007]. Second, rock bodies with more closely spaced defects yield finer grains when disaggregated [e.g., *Sammis et al.*, 1986], and finer grains are more frequently transported by fluid- and gravity-driven processes [e.g., *Gilbert*, 1877; *Davis*, 1899]. Defect spacing can vary dramatically across a landscape, and often reflects the inherited tectonic fabric of the landscape in question, and may ultimately lead to the formation of structurally controlled drainage and topography [e.g., *Koons et al.*, 2012; *Roy et al.*, 2016]. *Roy et al.* [2015] studied the first of these effects—that of varying rock resistance to disaggregation—and found theoretical support for the hypothesis that naturally occurring strength gradients have a strong influence on the development of drainage network patterns. More specifically, drainage network patterns tend to reflect the geometry of underlying active or inactive tectonic structures due to the more efficient erosion of preexisting fault-weak zones, causing channels to become structurally confined. Despite the scientific advances made by these arguments, there is still much left to be learned about the influence of rock mechanics on erosion rates and landscape evolution in general. Little is known about the influence of mechanical failure on the texture of sediments, and hence, whether variations in the size of sediment released by erosion of faulted rock versus erosion of intact rock are likely to have a significant influence on transport capacity.

In this paper, the results of *Roy et al*. [2015] are expanded upon to address the combined effects of rock strength and sediment texture by assuming that mechanical defects in bedrock take the form of fault-weakened zones, establishing a fracture spacing gradient that controls the heterogeneous distribution of both rock strength and initial sediment texture. Here we define strength in terms of rock cohesion and fracture spacing [*Hoek and Brown*, 1980] and texture as the volumetric fraction of sand in fractured rock and alluvial sediment [*Wilcock*, 1998]. We begin to explore the problem of mechanical heterogeneity in landscape evolution first with a motivating example of erosion in a fault-weakened zone in New Zealand. Measurements and observations from the field provide clues to help us design the theoretical framework for modeling heterogeneous rock strength and grain-size distributions in generalized landscape evolution models. Four previously studied phenomena are integrated into our models: (1) fluvial erosion rate scales inversely with bulk-rock plastic strength [e.g., *Sklar and Dietrich*, 2001, 2004], (2) the spacing of fractures and joints often exhibits power law scaling with implications for initial sediment texture upon erosion [e.g., *Jébrak*, 1997], (3) sediment transport rate scales inversely with grain diameter [e.g., *Wilcock*, 2001, 2005; *Wilcock et al*., 2009; *Julien*, 2010], and (4) the presence of sand enhances mobility of gravel, while the presence of gravel hinders the mobility of sand [*Wilcock*, 1998]. These phenomena are applied first in simple channel profile models of fluvial erosion and transport to better understand the basic longitudinal patterns of elevation and texture associated with heterogeneous rock strength and sediment texture. Further numerical experiments test the sensitivity of fluvial incision and transport to heterogeneous patterns of rock cohesion and texture across a landscape surface, with a specific interest in how the spatial distribution, texture, and residence time of sediments respond to different levels of rock weakening (also see our supporting information for storm sensitivity analysis). Our numerical results are meant to build field-testable theoretical predictions by studying the combined influence of mechanical defects using a combination of detachment-limited incision for bedrock and transport-limited flux for alluvium.

The planar weak zones in our models are meant to represent tectonically inactive structural features, but they could also potentially be used to represent other planar geologic features such as lithostratigraphic units, dikes, and sills that introduce local mechanical defects. However, it is advantageous to study the effects of fault-weakened zones over other lithological features because their presence introduces extremely sharp rock cohesion and texture gradients over a scale shared by channel width, their planar geometry is largely predictable or measurable in the field, and they are ubiquitous and well-documented structural feature [e.g., *Sibson*, 1977; *Sammis and Biegel*, 1989; *Ben-Zion and Sammis*, 2003; *Mooney et al*., 2007].

2. A Natural Example of Fault Erosion: Lewis Pass Region, New Zealand

2.1. Geological Background

The effects of heterogeneous rock strength on landscape evolution are apparent in the Lewis Pass region of the South Island of New Zealand, along a strand of the Fowlers Fault (Figure 1a) [*Rattenbury et al*., 2006]. The Fowlers Fault is one of a series of strike-slip faults that make up the Marlborough Fault System, a component of the Australian/Pacific Plate boundary that runs through the South Island of New Zealand [*Wilson et al*., 2004]. The Fowlers and associated faults cut through Torlesse greywacke [*Rattenbury et al*., 2006]. Many of these faults lie at the base of large valleys (Figure 1b) and are often concealed by thick alluvium. For this reason we choose to study a steep portion of the landscape, known as Henry Saddle, where the fault-weakened zone is not completely buried by alluvium (Figure 1b, Henry). The weak zone (Figure 1c) is oriented to the northeast and dips steeply to the northwest, and it is best exposed near the saddle indicated in Figure 1d. There is a fault gouge unit (Figure 1e) that is ~150 m wide and flanked by a cataclasite unit to the southeast (Figures 1f and 1g) and a more cohesive unit of jointed greywacke (Figures 1g and 1h) with widely spaced anastomosing shear zones to the west (Figure 1i). The drainage network pattern in this region tends to follow the strike of the weak zone (Figures 1c and 1j).

2.2. Rock Strength and Sediment Texture Summary

We estimated rock strength and texture using field measurements of cohesion and grain size, respectively. Cohesion was used as a proxy for rock resistance to detachment because it is a measureable form of plastic yield strength and because of its important role in the Mohr-Coulomb failure criterion [*Bieniawski*, 1974; *Brace and Kohlstedt*, 1980; *Hoek and Brown*, 1980, 1997; *Enlow and Koons*, 1998; *Schellart*, 2000]. Cohesion was estimated using the Hoek-Brown criterion [*Hoek and Brown*, 1980, 1997], based on measurements of the geological strength index (GSI), rock type, and field estimates of uniaxial compressive strength (UCS). GSI is a 0–100 scale

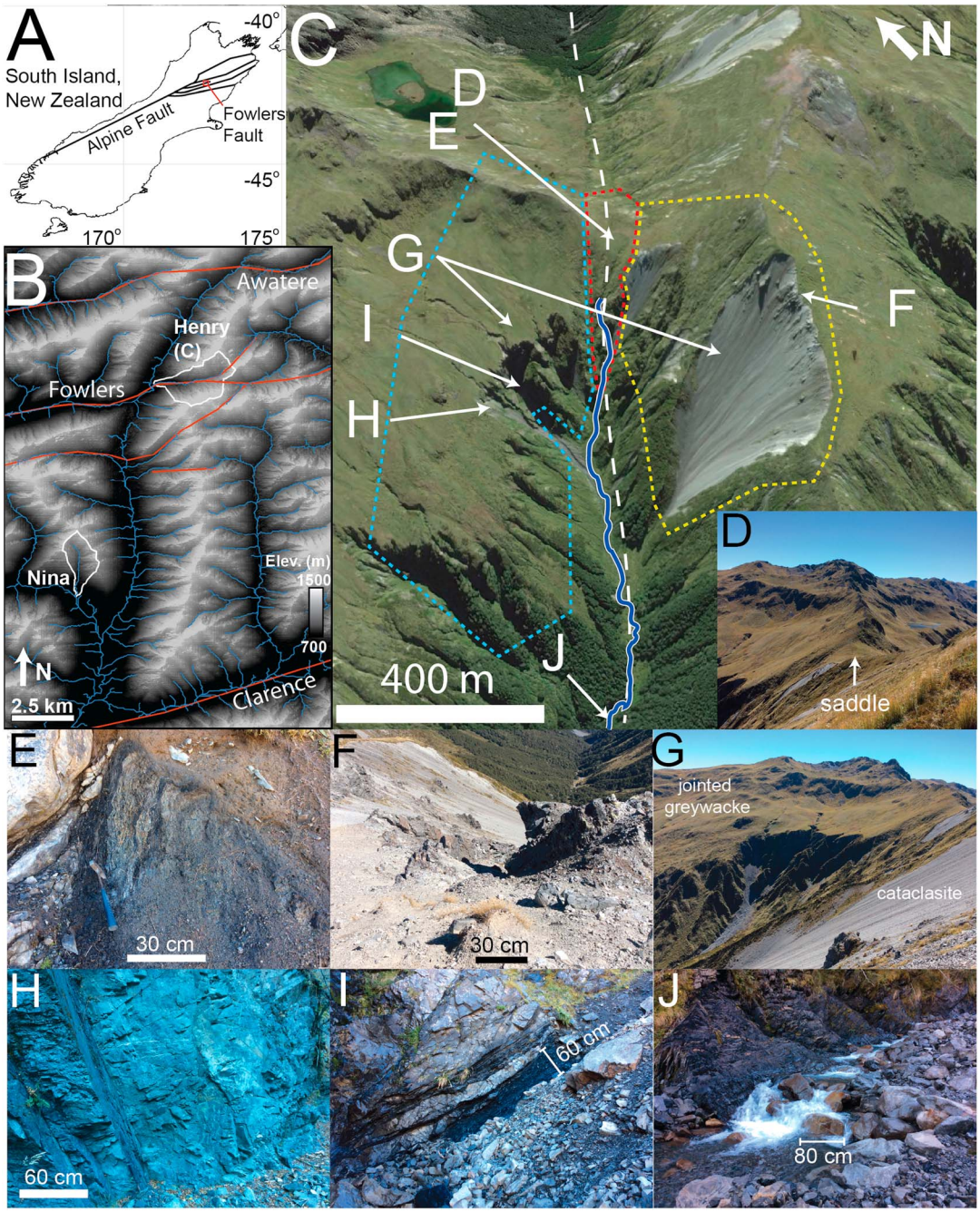

Figure 1. (a) Reference map. Red square indicates Lewis pass region and Fowlers Fault, South Island New Zealand. Black lines indicate trend of major tectonic structures. (b) Topography of Lewis Pass, rivers indicated in blue, major fault structures indicated in red [*Rattenbury et al.*, 2006]. White outlines: two watersheds used for slope-area analysis (Figure 2) are Henry Saddle (Henry) and Nina River Tributary (Nina). Topography data are distributed by the Land Processes Distributed Active Archive Center, located at the U.S. Geological Survey Center for Earth Resources Observation and Science http://LPDAAC.usgs.gov. (c) Henry Saddle, local channel (dark blue and white line) follows strike of weak zone (white dashed line). Polygons with dashed lines indicate observed local extent of exposed jointed greywacke (blue), cataclasite (yellow), and gouge (red) rock units. Rock is frequently covered by sediment farther downchannel, outside of colored polygons (source: 42°21′14.46″S, 172°26′53.68″E, Google Earth, imagery date 3 July 2010, accessed 1 March 2014). (d) Weak zone is exposed along a saddle. (e) Gouge unit exposed at the saddle, heavily eroded and fine grained. Valley walls are composed of (f and g) cataclasite, a relatively weak bedrock unit producing fine sediment and gravel, and (g and h) jointed greywacke, a relatively strong (i) bedrock unit that not only produces coarse gravel and boulders upon erosion but also contains weak argillite beds. Farther downchannel the structure is partially buried in (j) coarse alluvium, with an average grain size much larger than that of eroded fault gouge.

Table 1. Field Characterization of the Four Rock Types Including the Hoek-Brown Parameters Used to Estimate Cohesion and Median Grain Size

Rock Type	GSI	UCS Estimate	Rock-Type Parameter[b]	Cohesion (Pa)	Average Joint Spacing Range (mm)	Median Grain Size (mm)[c]
Jointed greywacke	55–80 Count[a]: 25	100–250	12	2.5×10^{7}–8.5×10^{6}	100–500	183 (55,320) Count[a]: 120 Skew: 2.6
Cataclasite	20–40 Count: 42	5–25	12	1.0×10^{5}–9.2×10^{5}	5–100	8.8 (1.9,18.9) Count: 121 Skew: 2.6
Gouge	5–15 Count: 9	0.25–1	12	2.8×10^{3}–1.7×10^{4}	<1	5.1 (0.3,8) Count: 243 Skew: 8.2
Downstream alluvium	-	-	-	-	-	19 (3.7,35) Count: 264 Skew: 3.8

[a]Count represents the number of samples taken to measure GSI and median grain size.
[b]Rock-type parameter is related to lithology; please refer to *Hoek and Brown* [1997].
[c]Values in parentheses represent one standard deviation below and above the mean value, respectively. The grain-size skewness calculated here is the moment coefficient of skewness [*Bulmer*, 2012].

measure of fracture spacing and quality with a versatile range that has proven useful as a field estimate of rock strength [e.g., *Hoek*, 1999; *Read et al*., 2000; *Brideau et al*., 2006]. Obtaining a truly representative estimation of rock type and UCS requires a rock sample size that is larger than the average spacing of fractures that allow the rock pieces to slide and rotate under different stress conditions [*Hoek and Brown*, 1997]. The rock-type parameter was taken from *Read et al*. [2000]. Joint spacing was measured directly in the field using a tape measure.

Results are displayed in Table 1. Fault gouge is by far the weakest bedrock unit, with a GSI range of 5–15. Gouge is so thoroughly disintegrated and chemically altered that it often has the consistency of clayey soil. Fracture surfaces are coated in soft, wet clay. The surrounding cataclasite is also relatively weak, with a GSI range of 20–40. However, fractures in the cataclasite tend to be dry, relatively rough, and uncoated, with little evidence for shearing or alteration except from landsliding (Figures 1e and 1f). The jointed greywacke to the northwest (Figure 1b) has a bulk GSI range of 55–80 (Figure 1g), punctuated by highly localized, submeter-scale shear zones with GSI range of 15–25 (Figure 1h). This rock unit provides the steepest relief in the region (Figure 1f).

We use our Henry Saddle field observations (Figure 1c), GSI measurements (Table 1), spatial data on fault geometry, and digital elevation models (Figure 1b) in order to explore the potential controls of rock cohesion and texture on slope and drainage area (Figure 2a). For comparison, we analyzed a tributary of the Nina River with similar drainage area that has no evidence of rock strength heterogeneity (Figure 2b). The relationship between slope and drainage area differs significantly between jointed greywacke and the fault-weakened zone at Henry Saddle (Figure 2c). Using a D8 flow routing algorithm, slope histograms display a significant division in median channel slope between the two rock units (Figure 2d). In general, the jointed greywacke unit hosts steep slopes and small drainage areas, while the damage zone tends to host lower slopes and a wider range of drainage areas (Figure 2c). Data from the Nina River tributary follow a pattern similar to the Henry Saddle jointed greywacke, and suggest a transition to fluvial processes at drainage areas of about 10^4 m^2 as indicated by the emergence of a negative slope-area trend [*Howard and Kerby*, 1983; *Montgomery and Foufoula-Georgiou*, 1993; *Sklar and Dietrich*, 1998]. Although debris flows are common in steep mountain basins, our subsequent modeling focuses on hillslope and fluvial transport (further discussed in section 3). For equal drainage area, slopes in the jointed greywacke are generally greater than slopes in the weak zone for both watersheds. These trends suggest that natural levels of rock damage can exert a sufficiently strong influence on landscape evolution to be reflected in the slope-area relationship.

Grain sizes were measured from loose material that showed evidence for recent separation from the fresh rock surface (Figures 1e, 1f, and 1i) and are strongly dependent on local fracture spacing in the source rock. Grain sizes in the alluvium, located downstream of where the rock units are exposed in steep hillslopes, were measured directly in the channel or along the channel banks (Figure 1j). We estimated the median grain size by measuring the intermediate axis of randomly chosen grains [*Wolman*, 1954] and use it only for relative comparison between rock units, and between the average joint spacing range for each rock unit. This method of grain-size measurement is subject to standard observer bias, but we maintained a consistent sampling technique between rock types. Fault gouge produces predominantly fine grained sediments upon erosion, whereas the average grain size for the cataclasite is greater, and the average size for the jointed greywacke is much greater (Table 1).

The gouge unit is predominantly covered by alluvium in all locations except at the drainage divide and intermittent locations along the reach of the channel (Figure 1j). Based on median values (Table 1), the

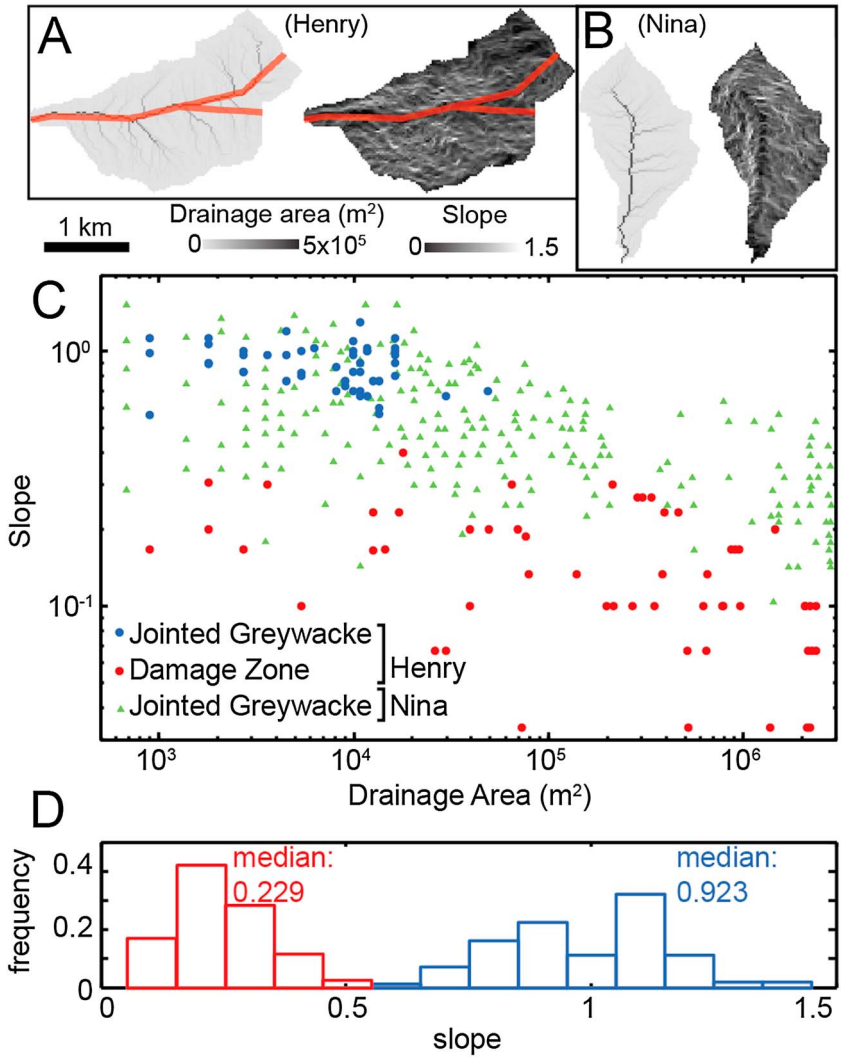

Figure 2. (a) Drainage area (m^2, left) and slope (m/m, right) data for Henry Saddle watershed (Figure 1c). Red areas indicate approximate extent of gouge unit. (b) Drainage area (left) and slope (right) data for Nina River tributary watershed with no apparent tectonic structures. (c) Slope versus area plot. Points represent single pixel locations in jointed greywacke (blue) and weak zone (red) of Henry Saddle, jointed greywacke (green triangle) of Nina River tributary. (d) Slope histogram for weak zone (red) and jointed greywacke (blue), Henry Saddle. Vertical axis is the slope frequency normalized by total sample size.

texture of the downstream alluvium is much coarser than the sediment produced from erosion of the underlying fault gouge but less coarse than boulders and cobbles that come from the jointed bedrock. The valley formed along the fault-weakened zone acts as storage for nearby sources of sediment.

These field observations suggest that fault-damaged rock is more easily eroded and produces fine-grained sediments that are more frequently transported by rivers. At the same time, adjacent rocks with a more intact structure resist erosion and produce coarse-grained sediments that often provide downslope armor over the damaged rock. Our field measurements provide clues to natural levels of rock cohesion and texture in eroding weak zones. In order to better understand the sensitivity of fluvial processes to rock strength heterogeneity, we apply a numerical approach to test if different degrees of rock weakening will affect drainage network evolution. Our numerical approach also allows us to examine how different degrees of fracture spacing will influence the sediment texture produced upon erosion, the evolution of sediment texture and bedrock exposure in channels, and the pattern of sediment storage across these landscapes. Below we explain our approach for examining the effect of rock properties on fluvial erosion and transport and provide a robust sensitivity analysis to determine the significance of rock damage on landscape evolution.

3. Modeling Methods

3.1. Surface Dynamics Model

We use the Channel-Hillslope Integrated Landscape Development (CHILD) model [*Tucker et al.*, 2001] to compute the erosion of bedrock and transport of sediment by fluvial and hillslope processes in a hypothetical terrain underlain by fault-damaged rock. The landscape surface is divided into irregularly discretized elements, each representative of a small equant area and connected to adjacent elements by a Delaunay triangulation [e.g., *Lee and Schachter*, 1980]. A steepest descent routing algorithm is used to calculate the spatial pattern of surface runoff accumulation over the discretized landscape surface. We use a general theory for mass continuity

$$\frac{\partial h}{\partial t} = F + H + U \tag{1}$$

where $\frac{\partial h}{\partial t}$ is time rate of change of land surface elevation ($\mathrm{L\,T^{-1}}$), F is the fluvial component of erosion or aggradation, H is the hillslope component of erosion or aggradation, and U represents all factors contributing to uplift or lowering of the surface relative to a base level. A lake-filling algorithm is used to find outlets if closed depressions exist in the model domain [*Tucker et al.*, 2001]. We use a combined rule set that treats fluvial transport F as either detachment limited over bedrock or transport limited over alluvium, depending on whichever is the largest of the two at a given time step and location:

$$F = \max(-D_c, \nabla q_c) \tag{2}$$

where D_c is the detachment capacity of exposed bedrock ($\mathrm{L\,T^{-1}}$), ∇q_c is the divergence of the bed load flux per unit area for the available surface grain size mix ($\mathrm{L\,T^{-1}}$), and max is the maximum function that selects the larger of the above two values. This approach means that a particular location within the model may be either detachment limited or transport limited and may change behavior over time in response to changes in topography, water discharge, sediment supply, and surface grain size [*Gasparini et al.*, 2004].

3.1.1. Bedrock River Incision

Bedrock channels frequently occur in high relief topography [*Howard and Kerby*, 1983; *Tucker and Slingerland*, 1996; *Sklar and Dietrich*, 1998; *Stock et al.*, 2005; *Attal et al.*, 2008, 2011]. We approximate the physics that control the rate of mechanical wear of bedrock by assuming that fluvial detachment capacity scales with unit stream power [e.g., *Seidl and Dietrich*, 1992; *Howard et al.*, 1994; *Stock and Montgomery*, 1999; *Whipple and Tucker*, 1999; *Tucker et al.*, 2001; *Hancock and Anderson*, 2002; *Whipple*, 2002, 2004; *Whittaker et al.*, 2007; *Yanites et al.*, 2010; *Attal et al.*, 2011]:

$$D_c = -k_{b(x,y,z)}\omega \tag{3}$$

where the fluvial contribution to erosion rate D_c at any point on a bedrock surface depends on spatially variable erodibility $k_{b(x,y,z)}$ ($\mathrm{L\,T^2\,M^{-1}}$) and stream power per unit width ω ($\mathrm{M\,T^{-3}}$). Note that the detachability of alluvium is assumed to be effectively infinite, while that of bedrock varies in space as described below. We assume that the average rate of channel-bed incision is proportional to stream power per unit width ω at every element:

$$\omega = \gamma\left(\frac{Q}{W}\right)S \tag{4}$$

where γ is the unit weight of water (9800 $\mathrm{kg\,m^{-2}\,s^{-2}}$), Q is water discharge ($\mathrm{L^3\,T^{-1}}$), W is channel width (L), and S is channel slope. Channel width W is calculated using the hydraulic geometry relationship [*Leopold and Maddock*, 1953; *Whipple*, 2004]:

$$W = k_w Q^b \tag{5}$$

where b is the width-discharge exponent, here given a value of 0.5, and k_w is the width-discharge coefficient, here given a value of $10\,\mathrm{s^{0.5}\,m^{-0.5}}$.

3.1.2. Fluvial Sediment Transport

Bedrock erosion produces sediment, the texture of which depends on the lithologic and mechanical properties of the bedrock, as discussed in section 2. We use a pair of bed load transport equations developed by *Gasparini et al.* [1999, 2004] for transport-limited alluvial channels. The transport model is based on the work of *Wilcock* [2001], who developed sediment transport laws for sand and gravel mixtures from field and flume

data [*Wilcock*, 1998]. In this approach, a two fraction model is used where the transport capacities for the gravel and sand fractions are given by

$$Q_{sg} = kf_g A^{0.95} S^{1.05} \left[1 - \frac{\tau_{cg}}{\rho g} n^{-0.6} P A^{-0.3} S^{-0.7}\right]^{4.5} \quad (6)$$

$$Q_{ss} = kf_s A^{0.95} S^{1.05} \left[1 - \frac{\tau_{cs}^{0.5}}{(\rho g)^{0.5}} n^{-0.3} P A^{-0.15} S^{-0.35}\right]^{4.5} \quad (7)$$

$$k = \frac{11.2 k_w^{0.1} P^{0.95} g^{0.5} n^{0.9}}{(s-1)g} \quad (8)$$

where Q_{sg} and Q_{ss} are the volumetric bed load fluxes for gravel and sand, respectively ($L^3 T^{-1}$), f_g and f_s are the fraction of gravel and sand, respectively, P is runoff rate ($L T^{-1}$), A is drainage area (L^2), n is Manning's roughness coefficient (here given a value of 0.03 ($T L^{-1/3}$)), ρ is water density ($M L^{-3}$), g is gravitational acceleration ($L T^{-2}$), s is the specific gravity of the sediment, τ_{cg} and τ_{cs} are critical shear stresses ($M L^{-1} T^{-2}$) for gravel and sand, respectively, and k is a parameter defined in equation (8).

The critical shear stresses for sand and gravel depend on grain size and the fraction of sand present in the bed material. The critical shear stress τ_c is calculated using a nondimensional reference shear stress τ_r^* [*Gasparini et al.*, 2004]:

$$\tau_c = \tau_r^* (\rho_a - \rho) g D \tan(\alpha) \quad (9)$$

where ρ_a is the density of sediment grains, D is the grain diameter (L), and α is the bed load friction angle with a value of 40° [e.g., *Wiberg and Smith*, 1987; *Fischenich*, 2001]. The value of τ_r^* depends on f_s, the fraction of sand present (Figure 3). Generally speaking, the presence of sand enhances the mobility of gravel, while the presence of gravel hinders the mobility of sand [*Wilcock*, 1998; *Gasparini et al.*, 1999, 2004]. If sand makes up less than one tenth of the alluvium, gravel creates an interlocking framework and hinders the transport of both grain sizes. Sand mobility therefore becomes a function of gravel mobility. The gravel framework becomes less influential for the range $0.1 < f_s < 0.4$, where a greater abundance of sand supports a matrix-dominated alluvium. For $f_s > 0.4$, the alluvium is largely sand matrix dominated, and there is a significant decrease in critical shear stress for both sand and gravel [*Wilcock*, 1998, 2001].

Mass conservation (equation (1)) is solved on a Voronoi/Delaunay grid using a finite-volume method [*Tucker et al.*, 2001; *Tucker and Hancock*, 2010]. For model cells in which the detachment capacity is greater than the local excess transport capacity, rate of change of local height depends on the difference between incoming sediment and the capacity to transport sediments

$$\nabla q_c = \frac{\sum_{i=1}^{2} Q_{si}^{\text{in}} - \sum_{i=1}^{2} Q_{si}^{\text{out}}}{a} \quad (10)$$

where $\sum_{i=1}^{2} Q_{si}^{\text{in}}$ ($L^3 T^{-1}$) is the sum of all gravel and sand discharge rates coming into the element, $\sum_{i=1}^{2} Q_{si}^{\text{out}}$ ($L^3 T^{-1}$) is the sum of all gravel and sand discharge rates leaving the element, i varies from 1 to 2 representing the two grain sizes, and a is the element area [*Gasparini et al.*, 2004]. Erosion and deposition are calculated independently for the gravel and sand fractions, and sediment-transport divergence is calculated using equation (10) along with the proportions of the two size classes in the streambed. We assume that the entire depth of sediment will mix over the time scales used in our experiments [e.g., *Gasparini et al.*, 2004].

3.1.3. Hillslope Processes

Hillslope processes, such as debris flow incision, are sensitive to the mechanical properties of rock [*Brideau et al.*, 2006, 2009; *Hsu et al.*, 2008; *Moore et al.*, 2009]. There is evidence of this at Henry Saddle, where the cataclasite unit appears to host a greater frequency of large debris flow events than the nearby jointed greywacke (section 2.2 and Figures 1c and 1g). It is also apparent that debris flows and landslides are the dominant form of erosion in these more resistant rock units, whereas fluvial processes dominate in the gouge unit. Despite the apparent mix of surface processes in the field, we are primarily focused on isolating the sensitivity of fluvial processes to rock strength heterogeneity and specifically from the reference frame of weakened rock. For simplicity, we approximate natural hillslope processes by a linear diffusion equation and assume uniform diffusivy

$$H = k_d \nabla^2 h \quad (11)$$

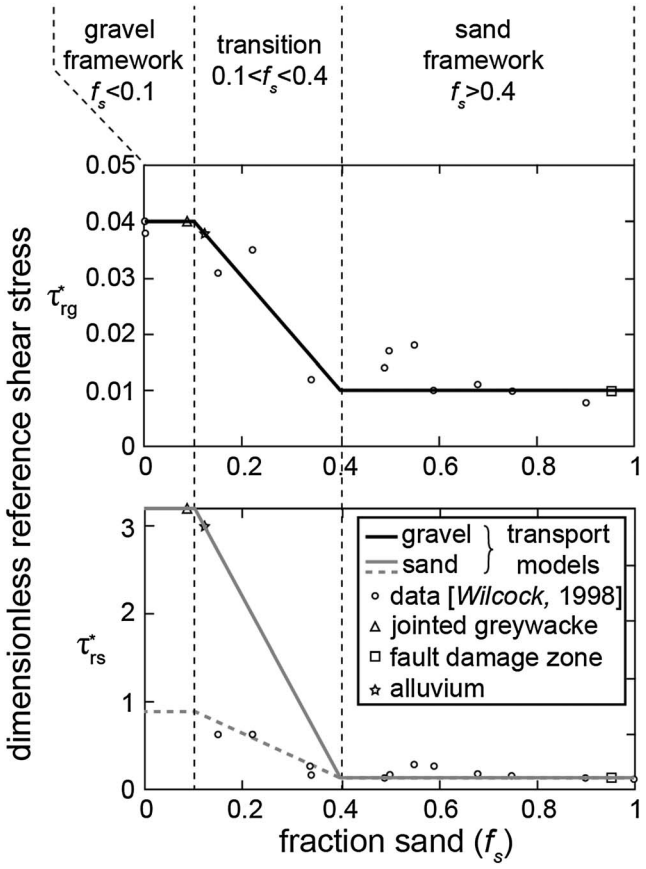

Figure 3. Dimensionless reference shear stress for (top) gravel and (bottom) sand (modified from *Gasparini et al*. [2004]). Circles represent data from *Wilcock* [1998]. Lines represent the transport model designed by *Wilcock* [1998] and adapted for stream power models by *Gasparini et al*. [1999]. Dashed black lines separate zones dominated by gravel framework, sand matrix, and the transition between the two. When $f_s < 0.1$, the dimensionless reference shear stress for sand $\tau^*_{rs} = (0.8D_g/D_s)\tau^*_{rg}$, where D_g is gravel diameter, D_s is sand diameter, and τ^*_{rg} is the dimensionless reference shear stress for gravel. This means that τ^*_{rs} in the range $f_s < 0.1$ will vary as a function of grain-size ratio; however, we maintain constant sand and gravel sizes for all experiments. All other dimensionless reference shear stress values are independent of grain size. The solid grey line shows the reference Shields stress for sand used in this paper; it is based on the results of *Wilcock* [1998] scald to our grain-size ratio of gravel to sand (D_g/D_s = 100). The dashed grey line is from *Gasparini et al*. [1999] and follows the experimental data of *Wilcock* [1998] for a smaller grain-size ratio (D_g/D_s = 20). Triangle, square, and star represent jointed greywacke, fault-weakened zone, and alluvium units, respectively, described in section 2 and explored analytically in section 3.3.

where k_d is a creep coefficient for alluvium (regolith) with a constant value of $10^{-3}\,\mathrm{m^2\,a^{-1}}$ and $\nabla^2 h$ is hillslope curvature with h equal to surface elevation (L). Creep only occurs in locations where soil thickness is greater than zero, with H limited to the available depth of soil.

3.1.4. Uplift Rate

The tectonic component of equation (1)

$$U = V_z + V_h \nabla h \tag{12}$$

is the sum of vertical rock motion relative to base level, V_z ($\mathrm{L\,T^{-1}}$), and lateral topographic advection, $V_h \nabla h$ ($\mathrm{L\,T^{-1}}$), which we prescribe as zero for our experiments. A steady, uniform rate of rock uplift relative to base level, 0.1 mm $\mathrm{a^{-1}}$, is used in order to represent a gently rising and completely exposed crustal basement. Submeter random noise is applied to the initial model relief in order to stimulate the development of a dendritic drainage pattern that strongly contrasts with the expected drainage pattern influenced by weak-zone erosion. Because the focus here is on erosion of inactive weak zones, none of the modeled weak zones allow for slip or further weakening.

3.2. Erodibility and Climatic Parameters

3.2.1. Rock Erodibility

We require erodibility and texture values for our landscape evolution models. The parameters we use are based on measurements from naturally occurring fault-weakened zones such as the one described in section 2 and from the efforts of others [*Thomson*, 1993; *Faulkner et al*., 2003, 2010; *Lockner et al*., 2009; *Mitchell et al*., 2011]. We assume that bedrock anelastic strength is inversely proportional to erodibility [*Sklar and Dietrich*, 2001, 2004] and use the cohesion-erodibility relation applied by *Roy et al*. [2015] and adapted from *Hanson and Simon* [2001]:

$$k_{b(x,y,z)} = k_c C^{-1/2}_{(x,y,z)} \tag{13}$$

where C is cohesion ($\mathrm{M\,L^{-1}\,T^{-2}}$) and k_c is a coefficient equal to 0.2 $\mathrm{m^{1/2}\,s\,kg^{-1/2}}$. Similar assumptions have been made for the erosion of cohesive soils [*Mirtskhoulava*, 1966, 1991; *Hanson and Simon*, 2001] in attempts to link the mechanical properties of the soils to erosion rates.

3.2.2. Rock Texture

Brittle failure governs the initial sediment texture that is introduced by the erosion of bedrock [e.g., *Molnar et al*., 2007]. Shear abrasion and tectonically inherited fractures are both potentially capable of generating

rock particle size distributions (PSDs) that can be fit to a power law curve with an inverse proportionality between grain size and the cumulative abundance of grains [e.g., *Sammis et al*., 1986; *Sammis and Biegel*, 1989; *Blenkinsop*, 1991; *Jébrak*, 1997; *Bonnet et al*., 2001; *Roy et al*., 2012]:

$$N(\geq D) = kD^{-\lambda} \tag{14}$$

where $N(\geq D)$ is the number of grains with median diameter $\geq D$, k equals $N(\geq 1)$, and λ is an exponent that determines the scaling of PSDs. In general terms, the likelihood of having grains $\geq D$ decreases as λ increases [*Jébrak*, 1997]. A strong argument for power law scaling of PSDs produced by the spacing and intersection of fractures is the lack of scale dependency in fracture growth processes above the molecular level [*Sornette and Davy*, 1991; *Bonnet et al*., 2001; *Saether and Ta'asan*, 2004]. The exponent λ can vary substantially between mechanisms and the number of fragmentation events [*Sammis et al*., 1986; *Blenkinsop*, 1991; *Jébrak*, 1997], it can be used to diagnose the fragmentation mechanism [*Jébrak*, 1997; *Barnett*, 2004; *Roy et al*., 2012], and because it is based on fracture spacing, varies sympathetically with rock cohesion [*Hoek and Brown*, 1980]. We define values for λ in section 3.4.

For example, almost all rocks with no deformation history exhibit a wide ambient fracture spacing associated with a possible combination of tectonically inherited fractures, exfoliation jointing, and bedding planes [e.g., *Bahat et al*., 1999; *Molnar et al*., 2007]. Infrequent fracture intersections are characterized by a relatively small scaling exponent λ, reflecting a low cumulative frequency of small grains at the expense of fractured coarse grains. Conversely, frequent shear abrasion events in fault-weakened zones drive grain-size reduction and increase the cumulative frequency of finer grains at the expense of disintegrating coarse grains [*Shelef and Oskin*, 2010; *Cappa et al*., 2014]. The degree of grain-size reduction increases significantly within meters from the ambient fracture spacing of intact rock to the core of a fault-weakened zone [e.g., *Ben-Zion and Sammis*, 2003]. Localized shear abrasion decreases fracture spacing and increases the scaling exponent λ with closer proximity to the primary slip surface, until the ambient fracture spacing signal is no longer discernable from the more pervasive shear abrasion mechanism.

The sediment transport model requires one population each of sand and gravel-sized grains, which we provide from our power law PSDs. The cumulative frequency of both grain sizes is calculated using equation (14), and then the raw number of grains of each size is calculated by subtracting the number of grains larger than the chosen grain size. Sand and gravel volumetric fractions are then calculated, assuming that all grains are spherical:

$$V = \frac{4}{3}\pi\left(\frac{D}{2}\right)^3 (N(\geq D) - N(\geq D + b)) \tag{15}$$

$$f_s = \frac{V_s}{V_s + V_g} \tag{16}$$

where b is the binning interval for D and V_s and V_g are the volumes of sand and gravel (L^3), respectively. These data are used to determine the volumetric ratio of sand to gravel-sized grains for use in the sand-gravel sediment transport model. We do not incorporate processes of comminution in our model. For the purposes of our experiments, sand and gravel diameters are 1 mm and 100 mm, respectively, and the binning interval is 0.1 mm. Our choice of gravel diameter falls under the cobble size range in terms of the Wentworth scale. The binning interval is necessary to make sure that our volume calculation for the sand grain size does not include the cumulative volume of grain sizes represented by gravel.

3.2.3. Storms

Discharge is calculated from the product of runoff rate and local contributing drainage area. Drainage area in turn is determined using a single-direction downslope routing algorithm [*Tucker et al*., 2001; *Tucker and Hancock*, 2010]. Discharge rates are fed by a temporally stochastic distribution of storm events associated with a rainfall intensity, a storm duration, and an interstorm duration chosen at random from exponential probability distributions [*Tucker and Bras*, 2000; *Sólyom and Tucker*, 2004]. Due to the large gap between climatic and geomorphic time scales, storm and interstorm durations are magnified such that average event spacing is 1000 years; this approach preserves the frequency distribution of discharge while improving computational efficiency [*Tucker et al*., 2001]. We set mean annual precipitation for our main experiments to 1 m a^{-1} and assume that storm events occur 10% of the time on average in order to replicate the typical climate around Lewis Pass [*Tomlinson and Sansom*, 1994]. Sediment transport rates are highly sensitive to the

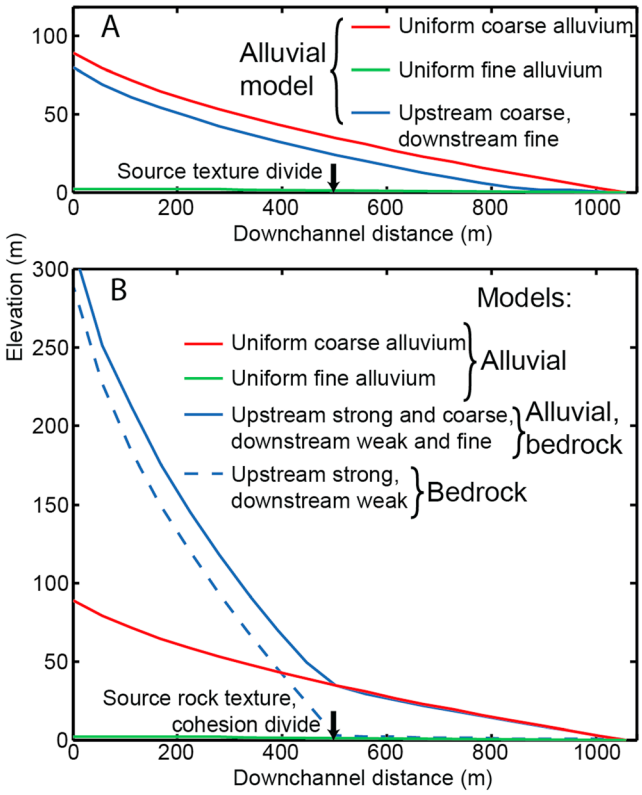

Figure 4. (a) Channel profiles for 1-D alluvial models. Red and green lines: uniform coarse and fine alluvium substrates, respectively. Blue line: channel crosses a source of coarse alluvium upstream and a source of fine alluvium downstream, both of which are uniformly uplifted and eroded. Location of the texture transition between sources is indicated by the black arrow. (b) Channel profiles for alluvial, bedrock, and combined fluvial erosion models. Dashed blue line: detachment-limited model in which channel traverses strong upstream bedrock and weak downstream bedrock. Solid blue line: mixed bedrock-alluvial fluvial incision and transport rules; channel traverses sources of strong, coarse-textured bedrock upstream and weak, fine-textured bedrock downstream.

frequency and magnitude of storm events [*Tucker and Bras*, 2000; *Molnar*, 2001; *Sólyom and Tucker*, 2004; *Tucker*, 2004; *Lague et al.*, 2005; *Molnar and Burlando*, 2005]; however, we choose to include our storm sensitivity analysis as supporting information to better focus our discussion on the main objectives of this paper.

3.3. Predicting Landscape Response

3.3.1. Alluvium Experiments

In this section we use the fluvial incision and transport equations described above to predict downstream changes in stream gradient, sediment thickness, and bed material texture as a channel traverses heterogeneous distributions of rock cohesion and texture. First, consider a simple comparison between two uniformly textured sources of alluvium with no underlying bedrock: one with a texture resembling the coarse-grained material produced upon the erosion of jointed greywacke in section 2 (9% 1 mm sand and 91% 100 mm gravel) and the other with a texture resembling the eroded fault gouge (95% 1 mm sand and 5% 100 mm gravel). From equations (1) and (2), we assume in this example that F is everywhere limited by ∇q_c (equation (10)) based on transport capacities of gravel (equation (6)) and sand (equation (7)). Using a 1-D version of CHILD and a linearly increasing downstream discharge, we determine channel slope and bed material texture for steady and uniform erosion into an infinitely deep alluvium with a constant uplift rate. The texture of the source alluvium remains constant, but the texture of sediment at the surface will evolve based on the upstream sediment source and transport capacity of the channel.

The model indicates an approximately sixteenfold contrast in channel gradient between profiles developed by the erosion of uniformly coarse (Figure 4a, red line) and fine (Figure 4a, green line) alluvium sources, respectively. Next, consider a channel that crosses a divide between an upstream source of coarse alluvium and downstream source of fine alluvium (Figure 4a, blue line). Under these conditions, the initial texture difference causes a transition in slope, but downchannel gravel aggradation beyond the gravel source causes the transition to occur ~400 m farther downstream than the textural divide of the source alluvium. The channel profile above this slope transition reflects the profile of the coarse alluvium model, while the downstream slope is similar to the fine-grained alluvium model. Much of the downstream fine-textured source alluvium is buried by transport of coarse alluvium from upstream. This reflects adjustment of size fractions in the bed material to allow transport of both fractions at the rate at which they are supplied [e.g., *Gasparini et al.*, 1999, 2004].

3.3.2. Bedrock and Mixed Bedrock-Alluvium Experiments

Now consider an experiment in which we assume the entire channel profile forms by fluvial incision into bedrock. In other words, we assume that F (equations (1) and (2)) is limited exclusively by D_c (equation (3)), and all

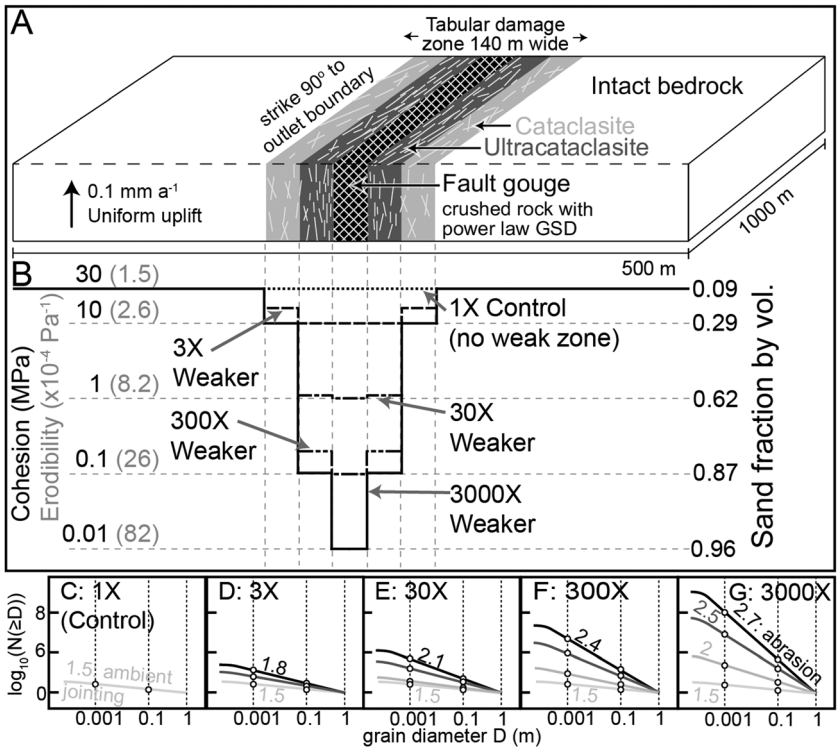

Figure 5. (a) Schematic illustration of the model geometry used for cohesion and texture sensitivity analysis (modified from *Roy et al.* [2015]). The weak zone dips vertically and strikes orthogonal to the outlet boundary (dashed boundary). The cohesion field is divided into four distinct units to create a symmetric cohesion gradient. From strongest to weakest the units are intact bedrock, cataclasite, ultracataclasite, and gouge. (b) Plot of cohesion versus fault width to represent the different modeled rock cohesion and texture gradients. Cohesion and erodibility values based on equation (13) are displayed on the left-hand axis for reference, and sediment texture data are shown on the right-hand axis. Five different cohesion gradients are used for sensitivity analysis. We refer to the magnitude difference between the intact bedrock and the gouge unit in the weak zone to differentiate each rock cohesion gradient. Cases range from control (1X), in which no weak zone exists and all bedrock has a uniform cohesion of 30 MPa, to 3000X, in which the gouge unit has a cohesion reduced by a factor of 3000, from 30 MPa to 10 kPa. The other weak zone units also reduce in cohesion to maintain the common gradient pattern. Also included are PSDs for the (c) control (1X), (d) 3X, (e) 30X, (f) 300X, and (g) 3000X experiments. Numbers on plot indicate value of λ based on fracture spacing for different rock units from the literature. Ambient tectonic jointing is the primary fragmentation mechanism in intact rock, which produces a relatively low λ value and relatively high proportion of coarse grains by volume. From 3X to 3000X the degree of fragmentation is increased, and the separation of λ values between intact bedrock and gouge becomes more significant. Shear abrasion is the dominant fragmentation mechanism in gouge, and the increase in λ represents an increase in the number of shear abrasion events that previously damaged the bedrock. Circles represent the two grain sizes used to represent the PSDs in the sand-gravel transport model.

detached sediments are immediately removed from the model domain. Under the same steady state conditions as in section 3.3.1, the channel erodes into an upstream source of strong jointed greywacke ($C = 1.7 \times 10^7$ Pa) and downstream source of weak fault gouge ($C = 9.9 \times 10^3$ Pa), leading to an approximately 42-fold difference in slope between the two rock units, occurring at the divide in source rock type (Figure 4b, dashed blue line).

Finally, we consider both alluvial transport and bedrock incision in our experiment so that F can be limited by ∇q_c or D_c (equation (2)). We apply a combined source rock cohesion and texture divide halfway down the channel profile, but we allow surface sediment texture to evolve based on transport and detachment capacity. Under these conditions (Figure 4b, solid blue line), carrying capacity across the jointed greywacke exceeds the supply produced by incision, and the upstream channel profile is similar to that of the previous experiment in which detachment capacity is rate limiting (Figure 4b, blue dashed line). Conversely, the downstream channel section resembles our uniform coarse alluvium model, rather than the low-relief profile that would be produced if bedrock detachment were the rate-limiting process (Figure 4b, red line). The downstream

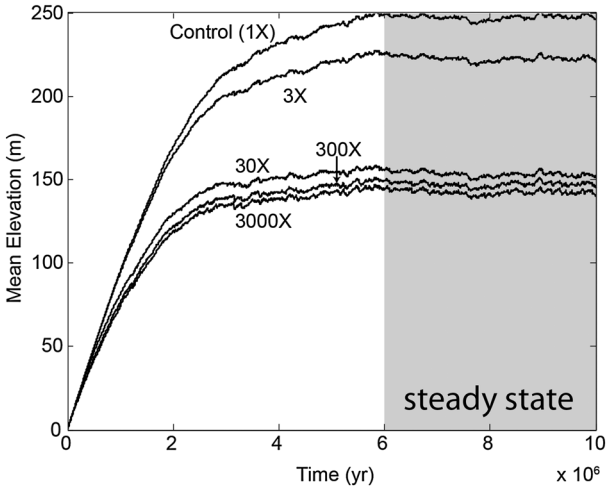

Figure 6. Plot of mean elevation over time for control (1X), 3X, 30X, 300X, and 3000X experiments. All experiments approach a condition in which mean height varies only slightly over time, which we interpret as a steady state condition (grey region). The model data displayed in Figure 7 (except elevation) are averaged over the steady state time interval.

channel profile is therefore largely shaped by the upstream source of coarse alluvium, not by the underlying weak bedrock, leading to a channel that is approximately 16 times steeper than it would be if erosion were limited only by the ability to detach weak cataclasite material. The alluvium texture is 10% sand, 90% gravel, which is very similar to the rock texture of the jointed greywacke.

These simple 1-D experiments provide basic information about channel profile shape across different lithological and alluvial conditions, but they do not take into account the 2-D distribution of drainage network patterns across a surface or the 3-D distribution of heterogeneous mechanical properties of rock. In order to more adequately predict the influence of weak zones on the drainage network pattern and the spatial distribution of sediments, we turn next to planform (2-D) models.

3.4. Landscape Evolution Models: Geometry, Initial, and Boundary Conditions

Figure 5a illustrates the generalized 3-D spatial pattern of lithology used in the landscape evolution model [*Ben-Zion and Sammis*, 2003; *Roy et al.*, 2015]. The model domain initially consists entirely of bedrock, with sediments being produced as the rock erodes. The topography is initially flat with a submeter-scale noise applied to the surface; a uniform uplift rate of 0.1 mm a^{-1} relative to base level is applied throughout each run. A single, vertically dipping zone of greater erodibility is located in the center of the model and strikes orthogonal to the flow outlet boundary on the southern terminus of the domain. The rock cohesion and texture gradients vary sympathetically and are discretized by dividing the weak zone width into parallel planar layers representing the transition from intact, crystalline bedrock to cataclasite, ultracataclasite, and fault gouge located at the center of the weak zone. We model a small watershed area with a mean grid resolution of 9 m in order to better represent the sharp gradient of rock strength that is typical for fault-weakened zones [*Ben-Zion and Sammis*, 2003].

Five experiments are run to test the sensitivity of surface processes to different rock cohesion and texture gradients; each represents a different increment of brittle failure, including a control experiment with homogeneous strength conditions. Cohesion in the gouge unit is 1X (control) to 3000X lower than that of the intact bedrock (Figure 5b). Rock texture gradients are based on power law PSDs for the dominant mechanisms of fragmentation (Figures 5c–5g), as explained in section 3.2.2. The scaling exponent λ is set to 1.5 for intact rock (Figure 5c) and increases with a greater degree of rock weakening (Figures 5d–5f) up to 2.7 for the gouge unit in the 3000X experiment (Figure 5g), representing a decrease in mean grain size produced upon erosion with greater proximity to the gouge unit. The entire weak zone is 140 m wide.

The experiments approach a steady state elevation condition before we conduct our sensitivity analysis. The use of storm events described in section 3.2.3 causes the steady state mean elevation to fluctuate within a narrow range (Figure 6). Due to these frequent storm-induced fluctuations, figures representing sediment texture, thickness, and cover are mean values taken after the model has stabilized within that narrow range of mean elevation.

4. Model Results

4.1. Topographic Pattern and Sediments

Results of the steady state experiments in Figures 7a–7e indicate that topography, and hence the drainage network pattern, reflects the presence of a weak zone, agreeing with the detachment-limited models of

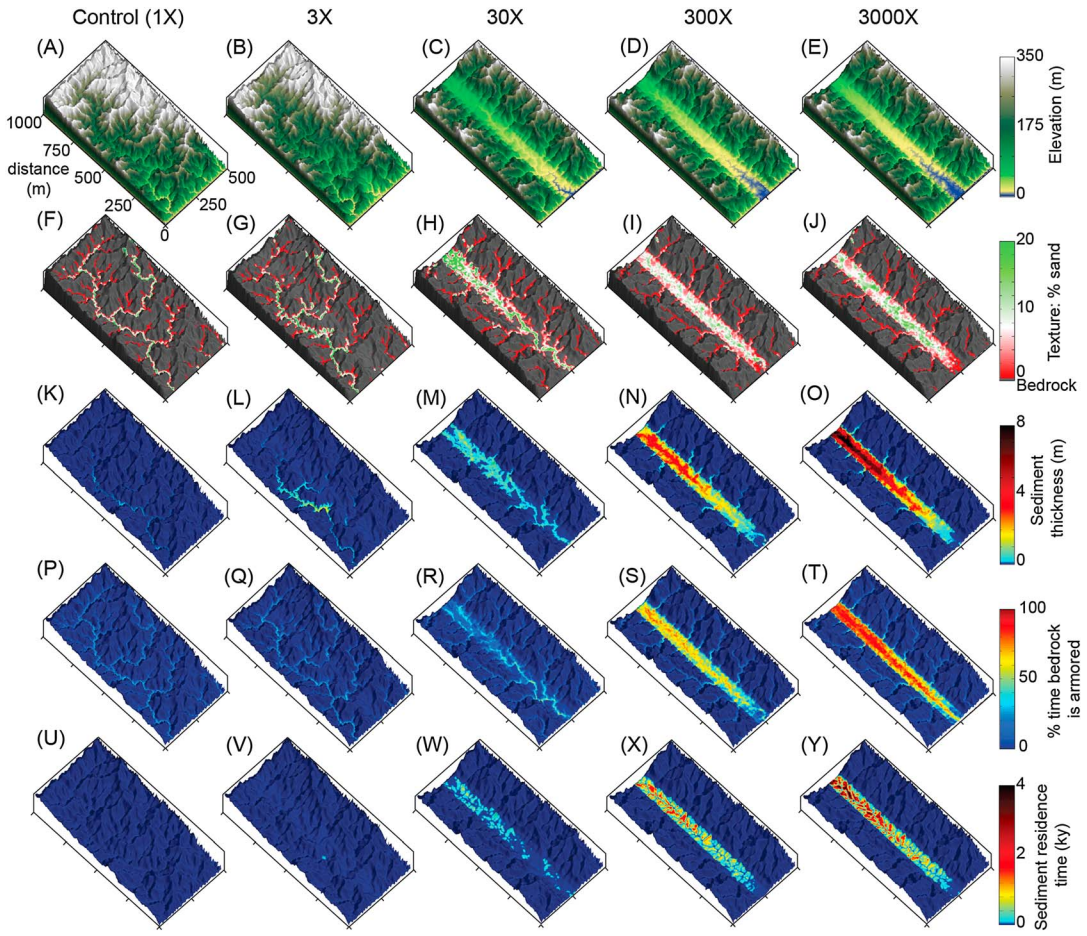

Figure 7. Experimental results. From left to right are control to 3000X experiments: (a–e) elevation maps, (f–j) sand fraction, (k–o) average alluvium thickness, (p–t) the percentage of time bedrock is covered by any alluvium thickness, (u–y) average residence time of alluvium. Averages taken over time interval are indicated in Figure 6.

Roy et al. [2015]. Despite this basic similarity, it is clear that in the experiments presented here, particularly those with large rock cohesion and texture gradients, the conditions within the weak zone can lead to a dominantly alluvial regime. In contrast, the control experiment (Figure 7a) is completely homogeneous and therefore shows no morphologic variations influenced by a cohesion gradient. In addition, channel conditions in the control experiment lead to detachment-limited behavior. The drainage pattern within the control is dendritic with no strong directional dependence. Sinuosity in the control experiment, measured as the ratio of channel-wise distance over straight line distance for the highest-order channel [*Hack and Young*, 1959; *Roy et al*., 2015], is 1.53 (Figure 8a). Bedrock is only rarely covered by relatively thin alluvium (Figures 7k and 7p and Figures 8c and 8e). Sediment texture becomes increasingly fine downstream, as a result of the bed material enrichment mechanism that *Gasparini et al*. [1999, 2004] described. The fine fraction tends to be less than 10%, which is roughly the texture contributed by erosion of the intact bedrock, and also represents the transition from a gravel framework to a sand matrix (Figures 7f and 8b). Sediment residence times, calculated as the volume of sediment divided by the average sediment flux for every element, approach zero (Figures 7u and 8e). A slope versus area plot for the control experiment (Figures 8f and 8i) shows that much of the bedrock remains exposed, and the relationship between channel slope and drainage area matches the expected trend for detachment-limited conditions. However, when drainage area exceeds ~3×10^4 m^2, the slope-area relationship diverges slightly from the pattern expected for strictly detachment-limited conditions (Figures 8f and 8i, black solid line).

The 3X experiment hosts a small cohesion gradient, causing tributaries and saddles to form in the location of the weak zone. However, the main channel crosses the cohesion gradient and is not strongly influenced by it, and sinuosity is still relatively high at 1.52 (Figure 8a). As with the control, sediments only occasionally cover bedrock

(Figures 7q and 8d) and thicknesses do not exceed 2 m (Figures 7l and 8c). The sediment texture field is similar to that of the control, except that there is a greater abundance of fine sediments, particularly where sediment thickness is greatest (Figure 7g). Sediment residence times are similar to the control (Figures 7v and 8e).

Topography produced from the 30X to 3000X cohesion gradient experiments indicates that the weak zones are reflected by straight, high-order channels while the surrounding intact bedrock hosts short, orthogonal tributaries of low order [*Roy et al.*, 2015]. The highest-order channels in the 30X and 300X experiments have sinuosity values of 1.24 and 1.15, respectively (Figure 8a). These experiments also show an increased prevalence of an alluvial regime overlying the weak zone. For the 30X to 3000X experiments, the weak zone is more easily eroded, and its local sediments are more readily transported by the high-order channel confined to the structure of the weak zone, leading to relatively low relief. Sinuosity is lowest in the 3000X experiment with a value of 1.05 (Figure 8a). However, erosion of the adjacent, more resistant bedrock produces an abundance of coarse-grained sediments that are transported down steep tributaries into the weak zone. Sediment thickness in the 3000X example can exceed 9 m above the weak zone (Figures 7o and 8c). From tributaries, the weak zone accumulates sediments that are much coarser than the rock textures of the weak zone itself (red patches, compare Figures 7h–7j and 8b to Figure 5b). The abundant coarse sediments continue to armor the weak zone (Figures 7m–7o and 8d) for the majority of steady state time (Figures 7r–7t). Armoring in the tributaries is minimal by comparison, and many of the coarse sediments produced by erosion are quickly deposited as small fans in the large valley, as can be seen by the red patches located at the bottom of the tributaries in Figures 7h–7j. The weak zone is less frequently exposed, sediment thicknesses are greater, and median sediment texture is slightly finer (Figure 8b) for larger cohesion gradient examples. The relationship between slope and drainage area for the 3000X experiment (Figures 7e and 7j) shows that only low-order tributaries are dominated by bedrock. Sediment residence times for the 30X experiment are noticeably larger than results from those in the control and 3X experiments (Figure 7w), and residence time continues to increase for the 300X and 3000X experiments (Figures 7x, 7y, and 8e).

Slope versus area plots for the 30X (Figures 8g and 8j) and 3000X experiments (Figures 8h and 8k) indicate that the intact rock unit rarely hosts drainage areas greater than 2×10^4 m^2. The slope-area relationship for the weaker rock units diverge from the expected trend predicted by the stream power rule, particularly for the 3000X experiment, but for equal drainage area, slopes in the weak rock remain lower than slopes in the intact rock.

5. Discussion

5.1. Drainage Network Pattern

The regional drainage network patterns in our sensitivity analysis reflect the local underlying rock cohesion and texture gradients when the gouge unit is $\geq$30X weaker than surrounding intact bedrock (Figures 7a–7e). For our experiments, weak bedrock takes the form of a straight corridor that steers surface runoff, leading to the formation of a straight, high-order trellis channel with orthogonal tributaries of low order (Figure 8a), similar to patterns seen in the Lewis Pass region (Figure 1b). Greater cohesion gradients lead to a greater attraction of surface runoff, but for cohesion gradients less than 30X the influence only occurs in low-order tributaries and hillslopes, while the main channel is largely unaffected. The control is not affected by a cohesion gradient and therefore produces a dendritic drainage pattern.

5.2. Aggradation in Structurally Confined Channels

5.2.1. Weak Zones and Sediment Storage

The relatively low bedrock relief in the model's fault-weakened zones leads to intermittent aggradation of coarse sediments. The alluvium thickness, percentage of time bedrock is armored, and the residence time of sediments, are all proportional to the magnitude of cohesion difference between intact rock and weak zone (Figures 8b–8e). Channel slopes in the model's weak zone exceed the equilibrium slope expected for detachment-limited channels, implying that alluvial transport capacity is the rate-limiting factor (Figures 8j and 8k). In other words, the channel is transport limited rather than supply limited, as seen by channel slope values exceeding the expected slope of fault gouge for equal drainage area. The tributaries that connect orthogonally to the structurally confined main stem channel cross the rock cohesion and texture gradients, bringing gravel downslope from steep bedrock channels into the low-relief weak zone (Figure 7).

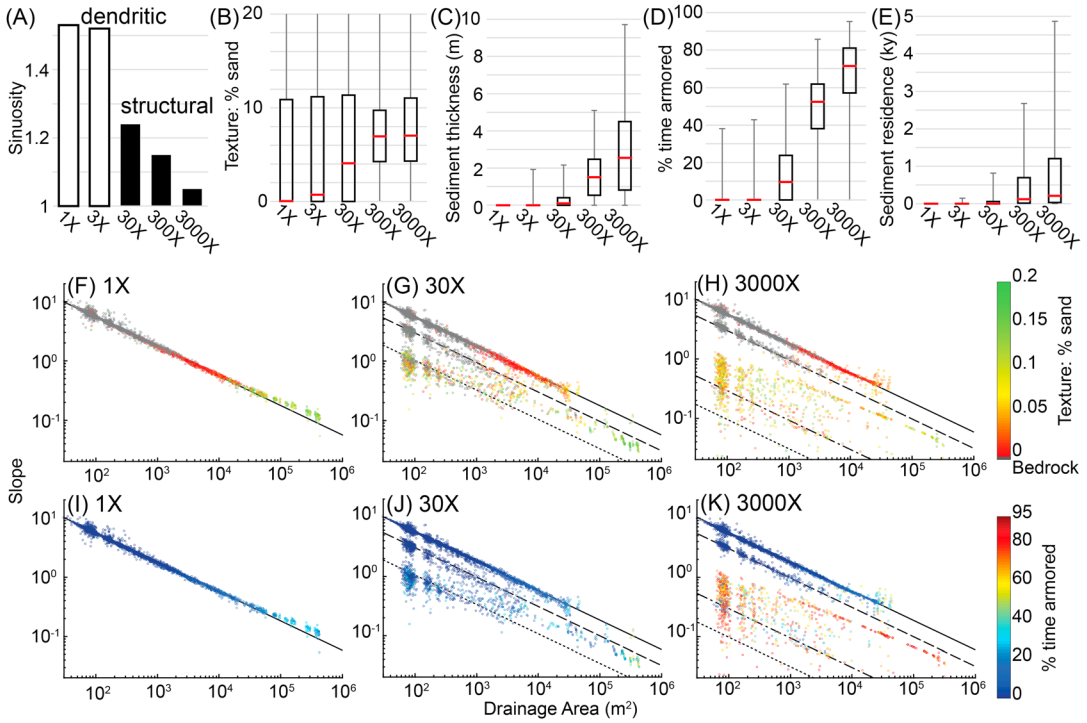

Figure 8. (a) Sinuosity of the main stem channel for each experiment. Bar color represents the basic drainage network pattern of dendritic (white) or structurally confined (black). (b) Box and whisker plot of sediment texture versus difference in rock cohesion, reporting the maximum and minimum values as whiskers, the interquartile range as the black box, and the median value as the red line for this and all following box and whisker plots. (c) Sediment thickness versus difference in rock cohesion, (d) percentage of time bedrock is armored versus difference in rock cohesion, and (e) sediment residence time versus difference in rock cohesion. All box plot data represent spatial distributions averaged over time, and reported values are taken from the main stem channel. (f–k) Slope (m/m) versus drainage area (m^2) plots for experiments control (1X) to 3000X. Colors represent sand fraction, grey color represents bedrock channels (Figures 8f–8h). Colors represent the percentage of time bedrock is covered by alluvium (Figures 8i–8k). Lines represent slope-area trends using the stream power equation for intact bedrock (solid), cataclasite (dashed), ultracataclasite (dash-dotted), and fault gouge (dotted).

Similar to our 1-D experiments in section 3.3, the sharp decrease in slope expected between intact bedrock and the gouge unit, up to ~55 times for the 3000X experiment, causes a sharp decrease in carrying capacity in the structurally confined channel (Figure 7j, red patches). The structurally confined channel attracts drainage from a relatively large area with multiple sources of coarse sediment (Figures 7a–7e). Coarse sediments aggrade above the weak zone in the 30X–3000X experiments, establishing an equilibrium slope dependent predominantly on the texture of incoming gravel alluvium, rather than on the erodibility of underlying bedrock (Figures 7h–7j). Armoring reduces the frequency of bedrock exposure, and frequency decreases with greater erodibility. Alluvium texture also scales with the magnitude of cohesion difference, indicating that a larger portion of sand is retained in alluvium when the underlying rock is weaker than the adjacent exposed bedrock. Despite this, the mean alluvium texture is still coarser than the underlying bedrock when there is a heterogeneous pattern of strength (compare Figure 8b to Figure 5b).

The relationship between channel slope and drainage area depends on the percentage of time that bedrock is covered by alluvium, and if it is often covered, the texture of the overlying sediment (Figures 8f–8h). For the weak zone, coarse sediments increase the steepness of the main channel to the point that channel slope becomes set by the flux and texture of alluvium rather than by the erodibility and texture of the underlying bedrock. This pattern of armoring is similar to that in the Henry Saddle watershed (Figure 1c). As discussed in section 2.2, the gouge unit in this watershed is frequently armored by coarse gravels derived from the erosion of the jointed greywacke unit (Figures 1c and 1j), but in contrast to our models, debris flows are the dominant form of transport through these stronger rock units. The sharp difference in slope between intact rock and the gouge unit follows the same trend as in our 30X to 3000X experiments, while the slope-drainage area relationship for the Nina River Tributary is similar to the control (1X) experiment. However, the lack of debris flow mechanism within the model leads to a different slope-area relationship than the natural watershed at the smallest drainage areas. Application of debris flow mechanisms and further work in strength-sensitive

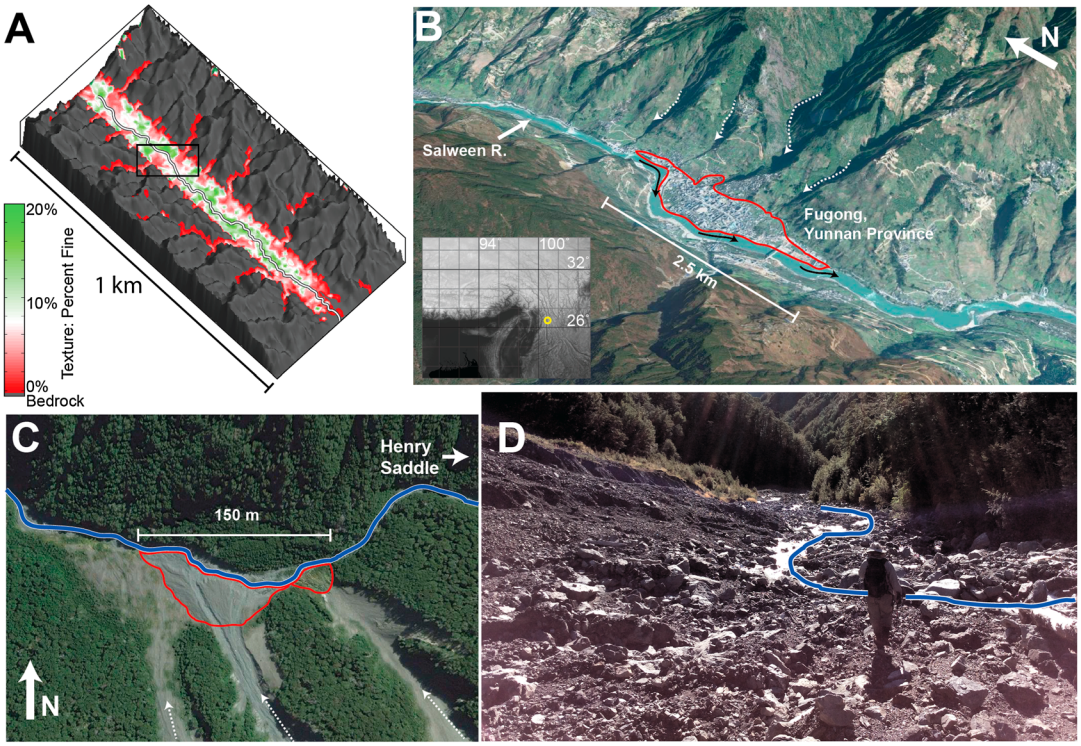

Figure 9. (a) Revisiting texture map of 3000X experiment. Black box indicates section of high-order, structurally confined channel deflected by coarse alluvial fans deposited by steep tributaries. (b) Along the Salween River, located at yellow dot on reference map of Eastern Himalayan Syntaxis, similar coarse alluvial fans form. Fugong alluvial fan, highlighted in red, is fed by steep bedrock tributaries indicated by dotted white lines. Black lines indicate flow direction of Salween River. (c) A reach of Henry Saddle Tributary downstream of site in Figure 1c that hosts an apparent deflection of flow around a series of large debris flows. Blue line indicates channel, fans highlighted in red, direction of debris flows indicated by white dashed lines. (d) Henry Saddle debris flow deposits (left) are coarse-grained gravels, cobbles, and boulders. Channel (blue line) has been noticeably deflected away from the fan toes (right). Picture taken looking west.

hillslope processes will be necessary to confidently interpret hillslope morphology in heterogeneous landscapes, but this is beyond the scope of this paper.

5.2.2. Downstream Fining and Coarse-Grained Fans

The modeled alluvial substrate fines downstream in tributaries, particularly at the major slope transition for tributaries that pass from intact bedrock to weak zone. Fans of coarse alluvium deposit at the confluence of the tributaries and the structurally confined channel (Figures 7f–7j) and cause a local increase in frequency of bedrock armoring (Figures 7p–7t). Sediment texture fining from tributary to main channel also correlates with an increase in the percentage of time bedrock is covered (Figures 7h–7j and 7m–7o), and both are due to the sharp transition in slope and the distance from the gravel sediment source. The path of the structurally confined channel is occasionally deflected by the coarse alluvial fans (Figure 9a), with a secondary influence on sinuosity after the primary structural influence (Figure 8a). Along the structurally confined channel the average alluvial texture is finer than in these coarse fans.

In nature it is common for rivers to bend around growing alluvial fans formed by tributaries with high sediment yield, such as the Fugong Fan along the Salween River (Figure 9b), or debris flows formed by mass hillslope failure, as is the case for the Henry Saddle field site (Figures 9c and 1c). Rock strength heterogeneity is one of many physical properties and processes that can cause the sediment supply of tributaries to exceed the capacity of the receiving channel. The Salween River, located in the Eastern Syntaxis of the Himalayas, is a large river that follows the damage zone of the Bangong-Nujiang tectonic suture [*Hallet and Molnar*, 2001; *Liu et al*., 2011]. Short, steep tributaries along the Salween deposit large amounts of coarse sediments in fluvial fans, such as the Fugong fan shown in Figure 10b, causing the path of the high-order river to deflect around the fan. Debris fans in the Henry Saddle field site, downstream of the region in Figure 1c, produce a similar pattern of deflection around the large gravel deposits (Figure 9d). Similar fluvial responses to large sediment pulses exist in the Navarro River [*Sutherland et al*., 2002; *Cui*, 2003] and Lava Falls on the Colorado

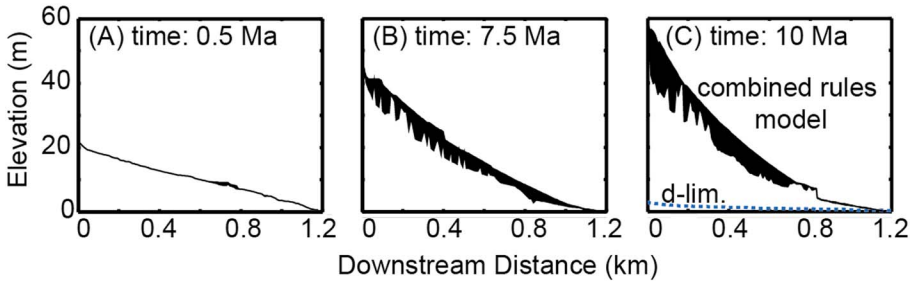

Figure 10. Longitudinal channel profiles for 3000X experiment: (a) time 0.5 Ma, (b) time 7.5 Ma, (c) time 10 Ma. Black area represents alluvium covering bedrock. Before approaching a steady state, few gravel sediments are transported from outside of the weak zone. Bedrock in the weak zone is largely exposed, and the sands produced by weak zone erosion have a short residence time. Tributaries begin to mobilize gravels by eroding the intact bedrock, causing them to armor the low-relief weak zone. Bedrock occasionally becomes exposed due to the steady and uniform uplift pattern. Dashed blue line is the profile of a detachment-limited experiment with an identical cohesion gradient.

River [*Webb et al*., 1999]. Other processes can lead to similar river bend patterns, such as meandering by lateral migration [e.g., *Leopold and Wolman*, 1960], but the mechanisms involved are not necessarily associated with a coarsening in sediment texture at the confluence of steep tributaries.

The model equations that we use to approximate landscape evolution create a simplified balance between uplift and erosion averaged over geologic time scales, yet by incorporating stochastic variations in discharge along with heterogeneous rock erodibility and texture, the model accounts for the formation of the short-term, transient alluvial fans. This pattern suggests that for our purposes, storm events are adequately approximated with a stochastic distribution and that the model equations provide sufficient theory to account for transitions between the rate-limiting fluvial processes of erosion and transport. However, a more detailed comparison between model results and field observations is required to provide further support, and this is beyond the limited scope of this paper.

5.2.3. Occasional Bedrock Exposure in the Weak Zone

Under steady state conditions, bedrock in the weak zone must occasionally become exposed and erode in order for bedrock erosion to keep pace (on average) with the uniform rate of rock uplift relative to base level. These model results agree with our observation that the highly erodible fault damage zone at Henry Saddle is occasionally visible (Figure 1j) downstream of the main exposure near the watershed divide. Figure 10 displays longitudinal profiles of the structurally confined channel in the 3000X experiment at three time steps. Based on our numerical experiments, eroded weak zones can provide significant sediment storage but the weak zone bedrock is expected to become exposed intermittently due to a constant rock uplift rate. Intermittent bedrock exposure can lead to intermittent knickpoint migration (Figure 10, time: 10 Ma) because upon exposure the channel slope exceeds the equilibrium slope of weak zone bedrock without alluvial armoring (Figures 8g and 8h and 8j and 8k). The armored bedrock will increase in slope in concert with the alluvium until sediments mobilize and the alluvium layer thins, exposing the weak bedrock for a relatively short duration. The irregular bedrock topography underlying the alluvium in the numerical experiments implies that the channel periodically avulses and then reincises whenever the bedrock becomes exposed, presumably creating epigenetic gorges that eventually become filled with alluvium from tributaries [e.g., *Ouimet et al*., 2007]. The frequency of bedrock exposure decreases upchannel in the weak zone and increases upchannel in the tributaries (Figures 7p–7t). However, based on our numerical experiments and our field observations, we suggest that in a natural setting, the intermittent exposure and incision of bedrock only plays a short-term role in the local evolution of channel slope in the weak zone, which is dominated instead by the upstream gravel source and its transportability.

These experimental results agree well with observations from the Peikang River in Taiwan. *Yanites et al*. [2011] noted that incision rates in the Peikang River are proportional to (1) the frequency of bedrock exposure and (2) stream power. This field analysis occurred after the 1999 Chi Chi earthquake, in which an excess of sediment was introduced from hillslopes into the river, increasing the average thickness of alluvium, decreasing the frequency of bedrock exposure, and subsequently decreasing incision rates [*Hsu et al*., 2010; *Yanites et al*., 2010, 2011].

5.2.4. Sediment Residence Time

The uniform rate of uplift relative to base level, combined with the fluvial erosion and transport processes, limits the residence time of armoring sediments in the weak zone (Figures 7u–7y). In these numerical

experiments, sediments are stored along the edges of the channel (small colored packets, Figures 7w–7y) and remain in place until the channel changes course. This pattern of sediment storage occurs in many different types of rivers [e.g., *Anderson and Anderson*, 2010], including at Henry Saddle (Figures 1j and 9d). Sediment residence time correlates with the relative rock cohesion and fracture spacing difference between weak zone and intact rock (Figure 8e). A greater relative difference reduces relief within the weak zone and allows for greater sediment volumes to accumulate during aggradation. Conversely, average sediment residence times in the control are negligible and agree with the extremely low percentage of time bedrock is covered by alluvium. This pattern is in agreement with our field observation that the strongest rock units are more frequently exposed. Residence times are greatest near where the weak zone intersects the northern boundary for the 30X to 3000X experiments, which reflects the tendency for bedrock exposure to initiate near the flow outlet boundary and intermittently migrate upchannel.

6. Conclusions

Our modeling of the lithologic controls on grain size and rock erodibility implies that drainage network patterns should be highly sensitive to the mechanical weakness, narrow fracture spacing, and persistent low relief associated with fault-weakened zones. Field observations of fault-weakened zone erosion in the South Island of New Zealand also suggest a strong sensitivity between rock damage, grain-size distribution, and erosion susceptibility. The sharp transition in rock erodibility and texture between intact and damaged rock can cause rivers to become structurally confined. Coarse gravel generated from erosion of steep bedrock channels leads to pervasive armoring of the low-relief weak zone. The alluvium that armors the weak zone is coarser than the sediments produced by its erosion, causing the relief within the structurally confined channel to increase as a function of alluvium texture, rather than the erodibility of the underlying rock. Occasionally, the damaged rock becomes exposed for short periods of time. This periodic exposure allows for continued incision of bedrock and reduces the residence time of sediments but has a negligible long-term influence on channel slope, and the eroded weak zones generally increase the capacity of rivers to store sediments.

Acknowledgments

The data used in this paper are available upon request from Samuel G. Roy (samuel.g.roy@maine.edu). This work was supported by NSF-EAR-1324637 to P.O. Koons and P. Upton and NSF-EAR-1323137 to G.E. Tucker. The manuscript benefitted from comments provided by the Editor, Associate Editor, and three anonymous reviewers, as well as discussions with C. Gerbi, D. Craw, and J. Howarth.

References

Anderson, R. S., and S. P. Anderson (2010), *Geomorphology: The Mechanics and Chemistry of Landscapes*, Cambridge Univ. Press, Cambridge, U. K.

Attal, M., G. E. Tucker, A. C. Whittaker, P. A. Cowie, and G. P. Roberts (2008), Modeling fluvial incision and transient landscape evolution: Influence of dynamic channel adjustment, *J. Geophys. Res.*, *113*, F03013, doi:10.1029/2007JF000893.

Attal, M., P. A. Cowie, A. C. Whittaker, D. Hobley, G. E. Tucker, and G. P. Roberts (2011), Testing fluvial erosion models using the transient response of bedrock rivers to tectonic forcing in the Apennines, Italy, *J. Geophys. Res.*, *116*, F02005, doi:10.1029/2010JF001875.

Bahat, D., K. Grossenbacher, and K. Karasaki (1999), Mechanism of exfoliation joint formation in granitic rocks, Yosemite National Park, *J. Struct. Geol.*, *21*(1), 85–96, doi:10.1016/S0191-8141(98)00069-8.

Barnett, W. (2004), Subsidence breccias in kimberlite pipes—An application of fractal analysis, *Lithos*, *76*(1–4), 299–316, doi:10.1016/j.lithos.2004.03.019.

Ben-Zion, Y., and C. G. Sammis (2003), Characterization of fault zones, *Pure Appl. Geophys.*, *160*, 677–715.

Bieniawski, Z. T. (1974), Estimating the strength of rock materials, *J. South African Inst. Min. Metall.*, *74*, 312–320.

Blenkinsop, T. G. (1991), Cataclasis and processes of particle size reduction, *Pure Appl. Geophys.*, *136*(1), 60–86.

Bonnet, E., O. Bour, N. E. Odling, P. Davy, I. Main, P. Cowie, and B. Berkowitz (2001), Scaling of fracture systems in geological media, *Rev. Geophys.*, *39*, 347–383, doi:10.1029/1999RG000074.

Brace, W., and D. Kohlstedt (1980), Limits on lithospheric stress imposed by laboratory experiments, *J. Geophys. Res.*, *85*, 6248–6252, doi:10.1029/JB085iB11p06248.

Brideau, M.-A., D. Stead, and R. Couture (2006), Structural and engineering geology of the East Gate Landslide, Purcell Mountains, British Columbia, Canada, *Eng. Geol.*, *84*(3–4), 183–206, doi:10.1016/j.enggeo.2006.01.004.

Brideau, M.-A., M. Yan, and D. Stead (2009), The role of tectonic damage and brittle rock fracture in the development of large rock slope failures, *Geomorphology*, *103*(1), 30–49, doi:10.1016/j.geomorph.2008.04.010.

Bulmer, M. G. (2012), *Principles of Statistics*, Courier Dover Publications, Mineola, New York.

Cappa, F., C. Perrin, I. Manighetti, and E. Delor (2014), Off-fault long-term damage: A condition to account for generic, triangular earthquake slip profiles, *Geochemistry*, *Geophys*, *Geosystems*, *15*(4), 1476–1493, doi:10.1002/2013GC005182.

Cui, Y. (2003), Sediment pulses in mountain rivers: 2. Comparison between experiments and numerical predictions, *Water Resour. Res.*, *39*(9 1240), doi:10.1029/2002WR001805.

Davis, W. M. (1899), The geographical cycle, *Geogr. J.*, *14*(5), 481–504.

Enlow, R., and P. O. Koons (1998), Critical wedges in three dimensions: Analytical expressions from Mohr-Coulomb constrained perturbation analysis, *J. Geophys. Res.*, *103*, 4897–4914, doi:10.1029/97JB03209.

Faulkner, D. R., A. C. Lewis, and E. H. Rutter (2003), On the internal structure and mechanics of large strike-slip fault zones: field observations of the Carboneras fault in southeastern Spain, *Tectonophysics*, *367*(3–4), 235–251, doi:10.1016/S0040-1951(03)00134-3.

Faulkner, D. R., C. A. L. Jackson, R. J. Lunn, R. W. Schlische, Z. K. Shipton, C. A. J. Wibberley, and M. O. Withjack (2010), A review of recent developments concerning the structure, mechanics and fluid flow properties of fault zones, *J. Struct. Geol.*, *32*(11), 1557–1575, doi:10.1016/j.jsg.2010.06.009.

Fischenich, C. (2001), Stability thresholds for stream restoration materials, *No. ERDC-TN-EMRRP-SR-29*, *Eng. Res. Dev. Cent. Vicksbg. MS Environ. LAB, ERDC-TN-EM*.
Gasparini, N. M., G. E. Tucker, and R. L. Bras (1999), Downstream fining through selective particle sorting in an equilibrium drainage network, *Geology*, *27*(12), 1079–1082, doi:10.1130/0091-7613(1999)027<1079:DFTSPS>2.3.CO;2.
Gasparini, N. M., G. E. Tucker, and R. L. Bras (2004), Network-scale dynamics of grain-size sorting: Implications for downstream fining, stream-profile concavity, and drainage basin morphology, *Earth Surf. Process. Landforms*, *29*(4), 401–421, doi:10.1002/esp.1031.
Gilbert, G. K. (1877), Report on the geology of the Henry Mountains, *U.S. Geogr. Geol. Surv. Rocky Mt. Reg., Washington, D. C.*
Hack, J. T., and R. S. Young (1959), Intrenched meanders of the north fork of the Shenandoah River, Virginia, *U.S. Geol. Surv. Prof. Pap., 354-A*, 10.
Hallet, B., and P. Molnar (2001), Distorted drainage basins as markers of crustal strain east of the Himalaya, *J. Geophys. Res.*, *106*, 13,697–13,709, doi:10.1029/2000JB900335.
Hancock, G. S., and R. S. Anderson (2002), Numerical modeling of fluvial strath-terrace formation in response to oscillating climate, *Geol. Soc. Am. Bull.*, *114*(9), 1131–1142.
Hanson, G., and A. Simon (2001), Erodibility of cohesive streambeds in the loess area of the midwestern USA, *Hydrol. Process.*, *38*, 23–38.
Hoek, E. (1999), Putting numbers to geology—An engineer's viewpoint, *Q. J. Eng. Geol. Hydrogeol.*, *32*(1), 1–19.
Hoek, E., and E. T. Brown (1980), *Underground Excavations in Rock*, Stephen Austin and Sons Ltd., London.
Hoek, E., and E. T. Brown (1997), Practical estimates of rock mass strength, *Int. J. Rock Mech. Min. Sci.*, *34*(8), 1165–1186, doi:10.1016/S0969-4765(04)00066-9.
Howard, A. D., and G. Kerby (1983), Channel changes in badlands, *Geol. Soc. Am. Bull.*, *94*, 739–752.
Howard, A. D., W. E. Dietrich, and M. A. Seidl (1994), Modeling fluvial erosion on regional to continental scales, *J. Geophys. Res.*, *99*, 13,971–13,986, doi:10.1029/94JB00744.
Hsu, H.-L., B. J. Yanites, C. Chen, and Y.-G. Chen (2010), Bedrock detection using 2D electrical resistivity imaging along the Peikang River, central Taiwan, *Geomorphology*, *114*(3), 406–414, doi:10.1016/j.geomorph.2009.08.004.
Hsu, L., W. E. Dietrich, and L. S. Sklar (2008), Experimental study of bedrock erosion by granular flows, *J. Geophys. Res.*, *113*, F02001, doi:10.1029/2007JF000778.
Jébrak, M. (1997), Hydrothermal breccias in vein-type ore deposits: a review of mechanisms, morphology and size distribution, *Ore Geol. Rev.*, *12*, 111–134.
Julien, P. Y. (2010), *Erosion and Sedimentation*, Cambridge Univ. Press, Cambridge, U. K.
Koons, P. O., P. Upton, and A. D. Barker (2012), The influence of mechanical properties on the link between tectonic and topographic evolution, *Geomorphology*, *137*, 168–180, doi:10.1016/j.geomorph.2010.11.012.
Lague, D., N. Hovius, and P. Davy (2005), Discharge, discharge variability, and the bedrock channel profile, *J. Geophys. Res.*, *110*, F04006, doi:10.1029/2004JF000259.
Lee, D. T., and B. J. Schachter (1980), Two algorithms for constructing a Delaunay triangulation, *Int. J. Comput. Inf. Sci.*, *9*(3), 219–242, doi:10.1007/BF00977785.
Leopold, L., and T. Maddock (1953), The hydraulic geometry of stream channels and some physiographic implications, *U.S. Geol. Surv. Prof. Pap.*, *252*, 57.
Leopold, L. B., and M. G. Wolman (1960), River meanders, *Geol. Soc. Am. Bull.*, *71*(6), 769–793, doi:10.1130/0016-7606(1960)71[769:RM]2.0.CO;2.
Liu, Y., M. Santosh, Z. B. Zhao, W. C. Niu, and G. H. Wang (2011), Evidence for palaeo-Tethyan oceanic subduction within central Qiangtang, northern Tibet, *Lithos*, *127*(1–2), 39–53, doi:10.1016/j.lithos.2011.07.023.
Lockner, D., H. Tanaka, H. Ito, R. Ikeda, K. Omura, and H. Naka (2009), Geometry of the Nojima Fault at Nojima-Hirabayashi, Japan—I. A simple damage structure inferred from borehole core permeability, *Pure Appl. Geophys.*, *166*(10–11), 1649–1667, doi:10.1007/s00024-009-0515-0.
Mirtskhoulava, T. E. (1966), Erosional stability of cohesive soils, *J. Hydraul. Res.*, *4*(1), 37–50, doi:10.1080/00221686609500091.
Mirtskhoulava, T. E. (1991), Scouring by flowing water of cohesive and noncohesive beds, *J. Hydraul. Res.*, *29*(3), 341–354, doi:10.1080/00221689109498438.
Mitchell, T. M., Y. Ben-Zion, and T. Shimamoto (2011), Pulverized fault rocks and damage asymmetry along the Arima-Takatsuki Tectonic Line, Japan, *Earth Planet. Sci. Lett.*, *308*(3–4), 284–297, doi:10.1016/j.epsl.2011.04.023.
Molnar, P. (2001), Climate change, flooding in arid environments, and erosion rates, *Geology*, *29*(12), 1071–1074, doi:10.1130/0091-7613(2001)029<1071:CCFIAE>2.0.CO;2.
Molnar, P., and P. Burlando (2005), Preservation of rainfall properties in stochastic disaggregation by a simple random cascade model, *Atmos. Res.*, *77*(1–4 SPEC. ISS), 137–151, doi:10.1016/j.atmosres.2004.10.024.
Molnar, P., R. S. Anderson, and S. P. Anderson (2007), Tectonics, fracturing of rock, and erosion, *J. Geophys. Res.*, *112*, F03014, doi:10.1029/2005JF000433.
Montgomery, D. R., and E. Foufoula-Georgiou (1993), Channel network source representation using digital elevation models, *Water Resour. Res.*, *29*, 3925–3934, doi:10.1029/93WR02463.
Mooney, W., G. Beroza, and R. Kind (2007), Fault zones from top to bottom: A geophysical perspective, in *Tectonic Faults Agents of Change on a Dynamic Earth*, edited by M. Handy, G. Hirth, and N. Hovius, pp. 24–61 , MIT Press, Cambridge, Mass.
Moore, J. R., J. W. Sanders, W. E. Dietrich, and S. D. Glaser (2009), Influence of rock mass strength on the erosion rate of alpine cliffs, *Earth Surf. Process. Landforms*, *34*, 1339–1352, doi:10.1002/esp.
Ouimet, W. B., K. X. Whipple, L. H. Royden, Z. Sun, and Z. Chen (2007), The influence of large landslides on river incision in a transient landscape: Eastern margin of the Tibetan Plateau (Sichuan, China), *Bull. Geol. Soc. Am.*, *119*(11–12), 1462–1476, doi:10.1130/B26136.1.
Rattenbury, M. S., D. B. Townsend, and M. R. Johnston (2006), Geology of the Kaikoura area. Institute of Geological and Nuclear Sciences 1:250000 geological map 13.1 sheet +70 p.
Read, S. A. L., L. Richards, and N. D. Perrin (2000), Assessment of New Zealand greywacke rock masses with the Hoek-Brown failue criterion, *GeoEng2000, Melb*.
Roy, S. G., S. E. Johnson, P. O. Koons, and Z. Jin (2012), Fractal analysis and thermal-elastic modeling of a subvolcanic magmatic breccia: The role of post-fragmentation partial melting and thermal fracture in clast size distributions, *Geochem. Geophys. Geosyst.*, *13*, Q05009, doi:10.1029/2011GC004018.
Roy, S. G., P. O. Koons, P. Upton, and G. E. Tucker (2015), The influence of crustal strength fields on the patterns and rates of fluvial incision, *J. Geophys. Res. Earth Surf.*, *120*, 275–299, doi:10.1002/2014JF003281.
Roy, S. G., P. O. Koons, P. Upton, and G. E. Tucker (2016), Dynamic links among rock damage, erosion, and strain during orogenesis, *Geology*, *44*(7), 583–586, doi:10.1130/G37753.1.
Saether, E., and S. Ta'asan (2004), *A Hierarchical Approach to Fracture Mechanics*, Hampton, Va.

Sammis, C. G., and R. L. Biegel (1989), Fractals, fault-gouge, and friction, *Pure Appl. Geophys.*, *131*(1/2), 255–271.
Sammis, C. G., R. H. Osborne, L. Anderson, M. Banerdt, and P. White (1986), Self-similar cataclasis in the formation of fault gouge, *Pure Appl. Geophys.*, *124*(1/2), 53–78.
Scheidegger, A. E. (1979), The principle of antagonism in the Earth's evolution, *Tectonophysics*, *55*, T7–T10.
Scheidegger, A. E. (2001), Surface joint systems, tectonic stresses and geomorphology: A reconciliation of conflicting observations, *Geomorphology*, *38*(3–4), 213–219, doi:10.1016/S0169-555X(00)00091-X.
Scheidegger, A. E. (2004), *Morphotectonics*, Springer, Berlin Heidelberg, Berlin.
Schellart, W. P. (2000), Shear test results for cohesion and friction coefficients for different granular materials: scaling implications for their usage in analogue modelling, *Tectonophysics*, *324*, 1–16.
Seidl, M., and W. Dietrich (1992), The problem of channel erosion into bedrock, *Catena, Supplement*, 101–124.
Shelef, E., and M. Oskin (2010), Deformation processes adjacent to active faults: Examples from eastern California, *J. Geophys. Res.*, *115*, B05308, doi:10.1029/2009JB006289.
Sibson, R. H. (1977), Fault rocks and fault mechanisms, *J. Geol. Soc. London.*, *133*, 191–213.
Sklar, L., and W. E. Dietrich (1998), River longitudinal profiles and bedrock incision models: Stream power and the influence of sediment supply, in *Rivers Over Rock: Fluvial Processes in Bedrock Channels, Geophys. Monogr. Ser.*, vol. 107, edited by K. J. Tinkler and E. E. Wohl, pp. 237–260, AGU, Washington, D. C.
Sklar, L. S., and W. E. Dietrich (2001), Sediment and rock strength controls on river incision into bedrock, *Geology*, *29*(12), 1087–1090.
Sklar, L. S., and W. E. Dietrich (2004), A mechanistic model for river incision into bedrock by saltating bed load, *Water Resour. Res.*, *40*, *W06301*, doi:10.1029/2003WR002496.
Sklar, L. S., C. S. Riebe, J. A. Marshall, J. Genetti, S. Leclere, C. L. Lukens, and V. Merces (2016), The problem of predicting the size distribution of sediment supplied by hillslopes to rivers, *Geomorphology*, doi:10.1016/j.geomorph.2016.05.005.
Sólyom, P. B., and G. E. Tucker (2004), Effect of limited storm duration on landscape evolution, drainage basin geometry, and hydrograph shapes, *J. Geophys. Res.*, *109*, F03012, doi:10.1029/2003JF000032.
Sornette, D., and P. Davy (1991), Fault growth model and the universal fault length distribution, *Geophys. Res. Lett.*, *18*, 1079–1081, doi:10.1029/91GL01054.
Stock, J., and D. R. Montgomery (1999), Geologic constraints on bedrock river incision using the stream power law, *J. Geophys. Res.*, *104*, 4983–4993, doi:10.1029/98JB02139.
Stock, J. D., D. R. Montgomery, B. D. Collins, W. E. Dietrich, and L. Sklar (2005), Field measurements of incision rates following bedrock exposure: Implications for process controls on the long profiles of valleys cut by rivers and debris flows, *Geol. Soc. Am. Bull.*, *117*(11/12), 174–194, doi:10.1130/B25560.1.
Sutherland, D. G., M. H. Ball, S. J. Hilton, and T. E. Lisle (2002), Evolution of a landslide-induced sediment wave in the Navarro River, California, *Bull. Geol. Soc. Am.*, *114*(8), 1036–1048, doi:10.1130/0016-7606(2002)114<1036:EOALIS>2.0.CO;2.
Thomson, R. (1993), Clyde Dam engineering geological completion report volume 1: Text and appendices, contract report C-1992/18, GNS Science, Avalon, NZ.
Tomlinson, A. I., and J. Sansom (1994), Rainfall normals for New Zealand for the period 1961 to 1990, NIWA Science and Technology Series Number 3, NIWA, Wellington.
Tucker, G. (2004), Drainage basin sensitivity to tectonic and climatic forcing: Implications of a stochastic model for the role of entrainment and erosion thresholds, *Earth Surf. Process. Landforms*, *29*, 185–205, doi:10.1002/esp.1020.
Tucker, G., and R. Bras (2000), A stochastic approach to modeling the role of rainfall variability in drainage basin evolution, *Water Resour. Res.*, *36*, 1953–1964, doi:10.1029/2000WR900065.
Tucker, G., S. Lancaster, and N. Gasparini (2001), The channel-hillslope integrated landscape development model (CHILD), in *Landscape Erosion and Evolution Modeling*, edited by R. S. Harmon and W. W. Doe, Kluwer Academic/Plenum Publishers, New York.
Tucker, G. E., and G. R. Hancock (2010), Modelling landscape evolution, *Earth Surf. Process. Landforms*, *35*(1), 28–50, doi:10.1002/esp.
Tucker, G. E., and R. Slingerland (1996), Predicting sediment flux from fold and thrust belts, *Basin Res.*, *8*, 329–349.
Webb, R. H., T. S. Melis, J. G. Griffiths, T. E. Elliot, R. J. Cerling, R. H. Wise, and J. Pizzuto (1999), Lava falls rapid in Grand Canyon: Effects of late Holocene debris flows on the Colorado River, *U.S. Geol. Surv. Prof. Pap.*, *1591*, 90.
Whipple, K. X. (2002), Implications of sediment-flux-dependent river incision models for landscape evolution, *J. Geophys. Res.*, *107*, 2039, doi:10.1029/2000JB000044.
Whipple, K. X. (2004), Bedrock rivers and the geomorphology of active orogens, *Annu. Rev. Earth Planet. Sci.*, *32*(1), 151–185, doi:10.1146/annurev.earth.32.101802.120356.
Whipple, K. X., and G. E. Tucker (1999), Dynamics of the stream-power river incision model: Implications for height limits of mountain ranges, landscape response timescales, and research needs, *J. Geophys. Res.*, *104*, 17,661–17,674, doi:10.1029/1999JB900120.
Whittaker, A. C., P. A. Cowie, M. Attal, G. E. Tucker, and G. P. Roberts (2007), Contrasting transient and steady-state rivers crossing active normal faults: New field observations from the Central Apennines, Italy, *Basin Res.*, *19*(4), 529–556, doi:10.1111/j.1365-2117.2007.00337.x.
Wiberg, P. L., and J. D. Smith (1987), Calculations of the critical shear stress for motion of uniform and heterogeneous sediments, *Water Resour. Res.*, *23*, 1471–1480, doi:10.1029/WR023i008p01471.
Wilcock, P. R. (1998), Two-fraction model of initial sediment motion in gravel-bed rivers, *Science*, *280*(5362), 410–412, doi:10.1126/science.280.5362.410.
Wilcock, P. R. (2001), Toward a practical method for estimating sediment-transport rates in gravel-bed rivers, *Earth Surf. Process. Landforms*, *26*(13), 1395–1408, doi:10.1002/esp.301.
Wilcock, P. R. (2005), Persistence of armor layers in gravel-bed streams, *Geophys. Res. Lett.*, *32* L08402, doi:10.1029/2004GL021772.
Wilcock, P. R., J. Pitlick, and Y. Cui (2009), Sediment transport primer: Estimating bed-material transport in gravel-bed rivers.
Wilson, C. K., C. H. Jones, P. Molnar, A. F. Sheehan, and O. S. Boyd (2004), Distributed deformation in the lower crust and upper mantle beneath a continental strike-slip fault zone: Marlborough fault system, South Island, New Zealand, *Geology*, *32*(10), 837–840, doi:10.1130/G20657.1.
Wolman, M. G. (1954), A method of sampling coarse river-bed material, *Trans. Am. Geophys. Union*, *35*(6), 951–956.
Yanites, B. J., G. E. Tucker, K. J. Mueller, Y. G. Chen, T. Wilcox, S. Y. Huang, and K. W. Shi (2010), Incision and channel morphology across active structures along the Peikang River, central Taiwan: Implications for the importance of channel width, *Geol. Soc. Am. Bull.*, *122*(7–8), 1192–1208, doi:10.1130/B30035.1.
Yanites, B. J., G. E. Tucker, H.-L. Hsu, C. Chen, Y.-G. Chen, and K. J. Mueller (2011), The influence of sediment cover variability on long-term river incision rates: An example from the Peikang River, central Taiwan, *J. Geophys. Res.*, *116*, F03016, doi:10.1029/2010JF001933.